CrossMark

J. Fluid Mech. (2016), *vol.* 792, *pp.* 67–97. © Cambridge University Press 2016
doi:10.1017/jfm.2016.61

Transition to turbulence in an oscillatory flow over a rough wall

Marco Mazzuoli[1,2] **and Giovanna Vittori**[1,†]

[1]Department of Civil, Chemical and Environmental Engineering, University of Genoa, Via Montallegro 1, 16145 Genova, Italy

[2]Institute for Hydromechanics, Karlsruhe Institute of Technology, 76131 Karlsruhe, Germany

(Received 16 June 2015; revised 1 December 2015; accepted 19 January 2016; first published online 29 February 2016)

A study of the oscillatory incompressible flow close to a wall covered with fixed rigid spheres is carried out by numerical means to provide information on unsteady flows over a rough wall. The simulations are carried out for two bottom configurations, characterized by different values of the diameter of the spheres and different values of the Reynolds number for a total of 10 cases. Three different flow regimes are identified as functions of both the Reynolds number and the diameter of the spheres. The force exerted by the flow on the spheres is discussed also in relation to the different flow regimes.

Key words: boundary layers, transition to turbulence

1. Introduction

Although oscillatory turbulent flows are often encountered in many different fields of practical relevance (e.g. coastal engineering, biological flows, turbo-machinery, etc.) and natural surfaces are often rough, many aspects of turbulence dynamics in oscillatory flows over a rough wall are still unknown because of the difficulties encountered in making accurate measurements of turbulence quantities in unsteady flows.

Numerical simulations, which could help in obtaining clear insight into the behaviour of both averaged quantities and turbulent fluctuations, are mainly limited to steady flows (see Jimenéz (2004) for a review). Only a few numerical investigations of oscillatory flows over a rough wall can be found into the literature.

Although in the present paper we focus our attention on the flow generated by an oscillating pressure gradient close to a rough wall, to mimic the boundary layer generated close to the bottom by the propagation of a surface wave, the results we describe are of general relevance.

Most studies of oscillatory boundary layers (Vittori & Verzicco 1998; Costamagna, Vittori & Blondeaux 2003; Ozdemir, Hsu & Balachandar 2014; Thomas *et al.* 2015) are devoted to studying the transition to turbulence and to determining the turbulence characteristics over a plane smooth wall.

† Email address for correspondence: vittori@dicca.unige.it

https://doi.org/10.1017/jfm.2016.61 Published online by Cambridge University Press

Blondeaux & Vittori (1994) showed that the presence of a waviness of small amplitude along the bottom surface can trigger a transition to turbulence for moderate values of the Reynolds number, because of a resonance mechanism. Later, Vittori & Verzicco (1998) and Costamagna *et al.* (2003) showed that wall imperfections play a significant role in the transition process, but turbulence characteristics for large Reynolds numbers are unaffected by the characteristics of the wall waviness. Ozdemir *et al.* (2014) investigated the combined effect of the nonlinearity and the amplitude of initial disturbances in the transition process in an oscillatory boundary layer. Thomas *et al.* (2015) investigated the effect of high-frequency disturbances of the flow field in the transition process to turbulence when the oscillatory flow close to a smooth plane wall is considered. Carstensen, Sumer & Fredsoe (2010) observed experimentally the appearance and development of turbulent spots in an oscillatory boundary layer when a transition to turbulence on a smooth wall takes place. The experimental observations of Carstensen *et al.* (2010) were confirmed by the direct numerical simulations of Mazzuoli, Vittori & Blondeaux (2011) who also quantified spot characteristics.

Among the experimental contributions to the study of oscillatory boundary layers over a naturally rough wall, it is worthwhile to mention the contributions of Sleath (1987), Jensen, Sumer & Fredsoe (1989) and recently that of Carstensen, Sumer & Fredsoe (2012). All of these contributions consider a natural rough wall. Sleath (1987) measured Reynolds stresses over beds that consisted of a single layer of sand, gravel or pebbles glued to a flat surface. He observed that, near the bed, the maximum value of the Reynolds stress was in phase with the first of the two peaks of turbulence intensity observed during the oscillatory cycle. However, moving far from the bed, the maximum of the Reynolds stress showed a 180° phase shift and was in phase with the second relative maximum of the turbulence intensity. A related effect was observed in the time-mean eddy viscosity. Sleath (1987) suggested that these phenomena are caused by the jets of fluid associated with the vortices shed by the roughness elements and ejected into the free-stream region. Jensen *et al.* (1989) carried out a set of experiments characterized by high values of both the Reynolds number and the roughness parameter. Close to the bed, they observed a significant increase, with respect to the smooth wall case, of both the turbulence intensity and the Reynolds stresses. By investigating the role of the roughness parameter, in accordance with Sleath (1987), they observed that an increase of the roughness size leads to an increase of the turbulence strength, since the momentum transfer is greatly enhanced by the eddies shed by the roughness elements.

More recently, Carstensen *et al.* (2012) carried out experiments at moderate values of the Reynolds number over a rough wall and observed that turbulent spots form, which are similar to those observed over a smooth wall (Carstensen *et al.* 2010). However, they observed the formation of turbulent spots for values of the Reynolds number smaller than those for which they observed turbulent spots over a smooth wall.

A first attempt to model the transition to turbulence in oscillatory flows over smooth and rough plane walls was made by Blondeaux (1987) by means of the two-equation turbulence model of Saffman (1970) and Saffman & Wilcox (1974). The model was shown to be able to describe both laminar and turbulent regimes and the transition process to turbulence. Blondeaux (1987) determined the critical conditions for the transition to turbulence over a plane wall, as a function of the roughness size, and found critical values of the Reynolds number of the same order of magnitude as those given by the empirical formulae suggested in the literature.

https://doi.org/10.1017/jfm.2016.61 Published online by Cambridge University Press

The literature cited so far deals with an oscillatory boundary layer over naturally rough walls. However, in order to get a more fundamental understanding of the role of roughness in triggering the transition to turbulence and determining turbulence characteristics, it is necessary to consider regular roughness elements.

Keiller & Sleath (1976) measured flow velocities close to rough beds oscillating in their own plane and considered both a regular roughness, made with spheres closely packed in a hexagonal pattern, and beds of gravel. During each half-oscillatory cycle they observed two maxima: one maximum was in phase with the maximum of the outer irrotational flow while the other maximum took place close to flow reversal. Moreover, they observed that the second peak was associated with strong vertical velocities and suggested that it was related to the shedding of vortex structures from the spheres glued to the bed.

Dixen *et al.* (2008) studied experimentally the oscillatory boundary layer over a bed made with spheres and found evidence that the ensemble and space-averaged velocity profiles follow the conventional logarithmic law during parts of the oscillatory cycle. Moreover, they considered different arrangements of the spheres and noticed that the friction factor, which is related to the bottom shear stress, was unaffected by the details of the roughness geometry.

Fornarelli & Vittori (2009) considered a rough bed made of half-spheres regularly placed on a plane wall and made direct numerical simulations of the flow field. The results of Fornarelli & Vittori (2009) agreed well with the experimental measurements of Keiller & Sleath (1976) both qualitatively and quantitatively. The numerical simulations showed that the flow is dominated by the vortex structures shed from the crests of the roughness elements, thus confirming the conjecture of Keiller & Sleath (1976). Moreover, during the accelerating phases, the formation of horseshoe vortices was observed at the base of the half-spheres. The dynamics of the free shear layers, which form at the top of the half-spheres, together with the presence of the horseshoe vortices, was found to have a relevant influence on the pressure distribution and on the forces exerted on the half-spheres. However, due to computational limitations, Fornarelli & Vittori (2009) could investigate only few cases. Recently, a paper has been published (Ghodke, Skitka & Apte 2014) which describes the results of a numerical investigation of the oscillatory flow over a geometry similar to one of the experiments by Keiller & Sleath (1976). In particular, Ghodke *et al.* (2014) considered spheres with a diameter equal to that of experiment 41 by Keiller & Sleath (1976) and identified the flow regime for values of the Reynolds number R_δ larger than 95 as 'fully developed turbulent', and suggested that the critical value of the Reynolds number for transition ranges between 95 and 150.

The present investigation is aimed at studying the oscillatory boundary layer that forms close to a rough wall covered with a regular roughness, made with spheres. Hence, the present geometry is more similar to the roughness elements used by Keiller & Sleath (1976) and Ghodke *et al.* (2014) than that used by Fornarelli & Vittori (2009). The numerical simulations are carried out for a range of Reynolds numbers larger than that considered by both Fornarelli & Vittori (2009) and Ghodke *et al.* (2014). Differently from Fornarelli & Vittori (2009) and Ghodke *et al.* (2014), two bed roughnesses, characterized by different diameters of the spheres, are considered. Compared with previous contributions, a more exhaustive investigation of the parameter space is made. Moreover, the present investigation provides a deeper insight into the transition process and allows the identification of three flow regimes depending on the value of the Reynolds number and the diameter of the spheres.

First, the problem and the numerical procedure are described. Then, a section is devoted to the validation of the results and to the description of the procedure used for

https://doi.org/10.1017/jfm.2016.61 Published online by Cambridge University Press

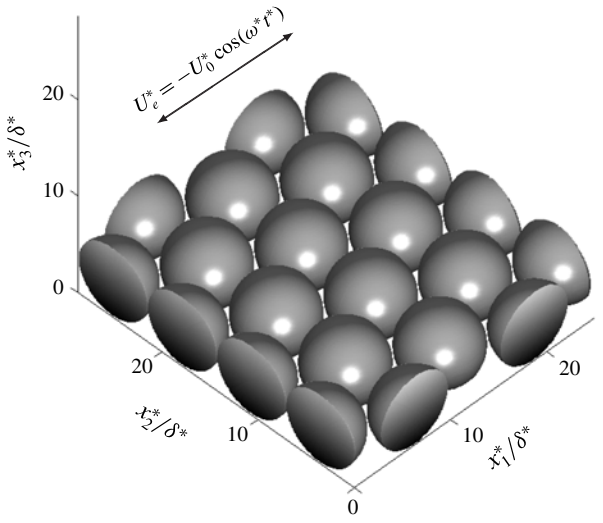


FIGURE 1. Sketch of the problem (configuration A, $D = 6.95$).

postprocessing. The third section, devoted to the discussion of the results, is divided into two parts. In the first part, the flow field is analysed with the aim of detecting the different flow regimes. The second part is devoted to the description of the forces acting on the spheres resting on the bed. Finally, conclusions are drawn in § 4.

2. The problem

A wall with a regular roughness made up of spheres lying on a flat surface and arranged in a hexagonal pattern (see figure 1) bounds a fluid of constant density ρ^* and kinematic viscosity ν^*. Hereafter, a star denotes dimensional quantities. A right-handed Cartesian coordinate system (x_1^*, x_2^*, x_3^*) is introduced. The origin of the Cartesian system is on the horizontal flat surface, the x_1^*- and x_2^*-axes lying on the wall, the x_3^*-axis being vertical and pointing upward.

The motion of the fluid, parallel to the wall, is generated by the harmonic temporal oscillations of the pressure gradient in the x_1^*-direction. The oscillation period T^* and the viscous length scale $\delta^* = \sqrt{(\nu^* T^*)/\pi}$ are taken as the characteristic temporal and spatial scales of the problem.

Even though, from a macroscopic point of view, the spheres can be though to rest on the plane wall and to be closely packed, the spheres in the computational box do not touch the plane wall but are $0.02D^*$ away from it, D^* being the sphere diameter. This small gap is required by the numerical implementation of the boundary conditions, which is presently carried out by using the immersed boundary method presented below.

For similar numerical reasons, a small gap exists between adjacent spheres. The distance (Δ_s^*) between adjacent spheres is a function of the number of grid points used in each run and is shown in table 1. The reader will notice small variations in the values of Δ_s used in the different runs, which are not expected to affect the results significantly.

Direct numerical simulations of continuity and Navier–Stokes equations are carried out. The dimensionless variables

https://doi.org/10.1017/jfm.2016.61 Published online by Cambridge University Press

D	R_δ	N	L_{x1}	L_{x2}	L_{x3}	Δ_s	Δ_{min}	Δ_{max}	Cycles
6.95	95.5	16	24.9	28.7	57.4	0.22	0.11	0.22	3
6.95	150	16	24.9	28.7	57.4	0.22	0.11	0.22	3
6.95	200	16	24.9	28.7	57.4	0.22	0.11	0.22	4
6.95	400	16	25.1	29.0	89.0	0.3	0.09	0.17	3
2.32	95.5	24	16.7	7.2	38.3	0.094	0.04	0.04	2
2.32	200	24	16.7	7.2	38.3	0.094	0.04	0.04	2
2.32	300	24	16.7	7.2	38.3	0.094	0.04	0.04	2
2.32	400	24	16.7	7.2	38.3	0.094	0.04	0.04	2
2.32	500	12	8.4	7.2	38.3	0.094	0.04	0.04	3
2.32	600	12	8.4	7.2	38.3	0.094	0.04	0.04	2

TABLE 1. The numerical parameters of the tests.

$$(x_1, x_2, x_3) = \frac{(x_1^*, x_2^*, x_3^*)}{\delta^*}, \quad t = \omega^* t^*, \tag{2.1a,b}$$

$$(u_1, u_2, u_3) = \frac{(u_1^*, u_2^*, u_3^*)}{U_0^*}, \quad p = \frac{p^*}{\rho^*(U_0^*)^2} \tag{2.2a,b}$$

are introduced, where U_0^* and $\omega^*(= 2\pi/T^*)$ are the amplitude and the angular frequency of the velocity oscillations far from the wall respectively. The dimensionless fluid velocity far from the wall turns out to be

$$(u_1, u_2, u_3)_{x_3 \to \infty} = (-\cos(t), 0, 0) \tag{2.3}$$

and is induced by an oscillating pressure gradient out of phase with (2.3) and with amplitude equal to $\rho U_0 \omega$.

The boundary conditions force the no-slip condition at the solid boundaries, periodic conditions along the x_1- and x_2-directions and the free-slip condition at the upper boundary of the computational domain ($x_3 = L_{x3}$).

Two bottom configurations are considered, characterized by different values of $D = D^*/\delta^*$. The first configuration (configuration A) consists of a layer of spheres, packed in a hexagonal pattern, with a diameter equal to $6.95\delta^*$ (see figure 1). In the second configuration (configuration B), smaller spheres, with a diameter equal to $2.32\delta^*$ and arranged in a hexagonal pattern, are considered. Values of the Reynolds number $R_\delta = U_0^*\delta^*/\nu^*$ ranging from moderate values, such that a laminar flow is observed, up to higher values, such that the flow is turbulent, are considered. The parameters of configuration A with $R_\delta = 95.5$ correspond to those of experiment number 41 by Keiller & Sleath (1976), and the run was used to validate the numerical approach and the postprocessing procedure.

A second-order semi-implicit method is used to advance the incompressible Navier–Stokes equations in time. A fractional-step method is employed where convective and diffusive terms are discretized by using third-order Runge–Kutta and Crank–Nicolson schemes respectively. Standard centred second-order finite-difference approximations are used for spatial derivatives.

In order to increase the grid resolution in the region of the computational domain closer to the spheres, the adaptive mesh refinement (AMR) technique (Vanella, Rabenold & Balaras 2010) is introduced. The refined grid has an oct-tree structure with a minimum grid size (Δ_{min}) in the region of the computational domain closer to

https://doi.org/10.1017/jfm.2016.61 Published online by Cambridge University Press

the spheres and a larger grid size (Δ_{max}) in the remaining part of the computational domain. The forcing of the no-slip condition at the surface of the roughness elements is obtained by means of the immersed boundary method by Uhlmann (2005). The immersed boundary method allows a vanishing velocity to be forced on the sphere surface by adding an appropriate forcing term to the discretized Navier–Stokes equations. As a consequence, the governing equations can be numerically integrated on a Cartesian grid without the need to introduce curvilinear coordinates. The AMR technique requires the use of specific multigrid solvers both for the Helmholtz and for the Poisson problems, which arise from the prediction step of the fractional-step scheme and from the continuity equation respectively. The multigrid solvers of both the Helmholtz and Poisson problems are based on the iterative algorithm by Huang & Greengard (1999). In particular, the Helmholtz solver uses the alternating direction implicit (ADI) approximate factorization and a 'local' direct solver that was specifically developed (M. Mazzuoli and M. Uhlmann, personal communication). The Poisson solver uses a pseudospectral approach and the 'local' direct solver developed by Ricker (2008) and implemented by means of routines of the FLASH code. The dimensions of the computational domain in the streamwise, spanwise and cross-stream (vertical) directions are denoted by L_{x1} ($L_{x1} = L^*_{x1}/\delta^*$), L_{x2} ($L_{x2} = L^*_{x2}/\delta^*$) and L_{x3} ($L_{x3} = L^*_{x3}/\delta^*$) respectively. The values of L_{x1}, L_{x2} and L_{x3} as well as the number of grid points and the number of spheres N vary from one run to another depending on the values of the dimensionless controlling parameters. The size of the computational box and the number of grid points are chosen by means of a compromise between the accuracy of the results and the computational resources required to obtain them. In order to verify that the size of the computational box was adequate, the two-point correlation of the fluctuating components of the velocity field was considered and it was verified that it tends to vanish as the two-point separation increases (see figure 2).

The adequacy of the number of grid points was verified by considering the 2D spectra of the specific turbulent kinetic energy at different distances from the crests of the spheres. Figure 3, which shows an example of the obtained 2D spectra, allows one to appreciate that the amplitude of the harmonics with large wavenumbers vanishes.

At least two full oscillatory cycles are simulated for all cases and the results of the first cycle are discarded, since they are affected by the initial conditions. It is worthwhile to mention that not all of the obtained flow fields are statistically steady. For this reason the discussion of the results is not based on quantitative values derived from averaged quantities. The values of the parameters of the different runs are given in table 1.

The tests at the highest Reynolds number ($R_\delta = 600$) required $O(70\,000)$ time steps per period. The direct numerical simulations of the tests with configuration A were made on two different machines: a 24-core machine (DICCA) and the cluster machine IC2 (KIT Steinbuch Centre for Computing (SCC), Karlsruhe, Germany), requiring approximately 500k CPU hours in total. The tests with configuration B were performed on the BG/Q machine FERMI (CINECA, Bologna, Italy), requiring 1.9 M CPU hours over 1024 cores. The numerical code was designed to efficiently perform on these machines.

3. The results

3.1. *Code validation and processing of the results*

To validate the numerical code, a first run was made by fixing the diameter of the spheres and the value of the Reynolds number equal to those of experiment number

https://doi.org/10.1017/jfm.2016.61 Published online by Cambridge University Press

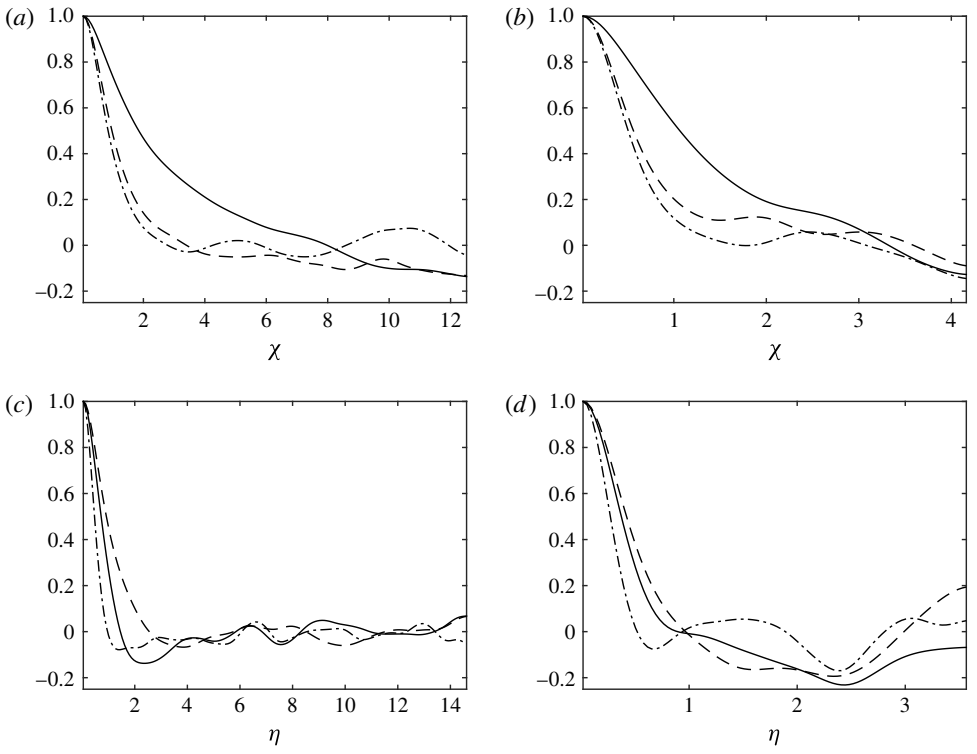


FIGURE 2. The two-point correlation of the fluctuating velocity components (χ = streamwise distance, η = spanwise distance). (*a*,*c*) Configuration A, $R_\delta = 400$, $t = 5.06\pi$, distance from the crests of the spheres equal to 0.0372δ. (*b*,*d*) Configuration B, $R_\delta = 600$, $t = 4.03\pi$, distance from the crests of the spheres equal to 0.0184δ. (*a*,*b*) Correlation along the streamwise (x_1) direction. (*c*,*d*) Correlation along the spanwise (x_2) direction. Solid line = streamwise velocity, broken line = cross-stream velocity, dash-dot line = spanwise velocity.

41 of Keiller & Sleath (1976). To compare the numerical results with the original measurements of Keiller & Sleath (1976), which were made by using a stationary probe over an oscillating rough bed, in our simulations the numerical probes were oscillated with the outer irrotational velocity. Moreover, since Keiller & Sleath (1976) measured the time development of the modulus of the velocity vector projected on a vertical plane parallel to the direction of the oscillating fluid (indicated with $|V|$), the same quantity was evaluated.

Figure 4(*b*) shows the experimental measurements of Keiller & Sleath (1976), while (*a*) shows the output of the numerical velocity probes, located at distances from the sphere crests equal to the distances used by Keiller & Sleath (1976).

Both the measurements of Keiller & Sleath (1976) and the numerical results show that the velocity close to the bed is characterized by high-frequency oscillations which are related to the passage of the probes over different spheres. Incidentally, let us point out that, for $R_\delta = 95.5$, the number of spheres passing the measurement points during a half-stroke is equal to $U_0^*/(\omega^* \Delta_{x1}^*) = 3.84$ ($\Delta_{x1}^* = 12.43\delta^*$ is the distance between the sphere crests along the streamwise direction). The maximum value of $|V|$ is in phase with the maximum of the outer velocity, which oscillates sinusoidally in time.

https://doi.org/10.1017/jfm.2016.61 Published online by Cambridge University Press

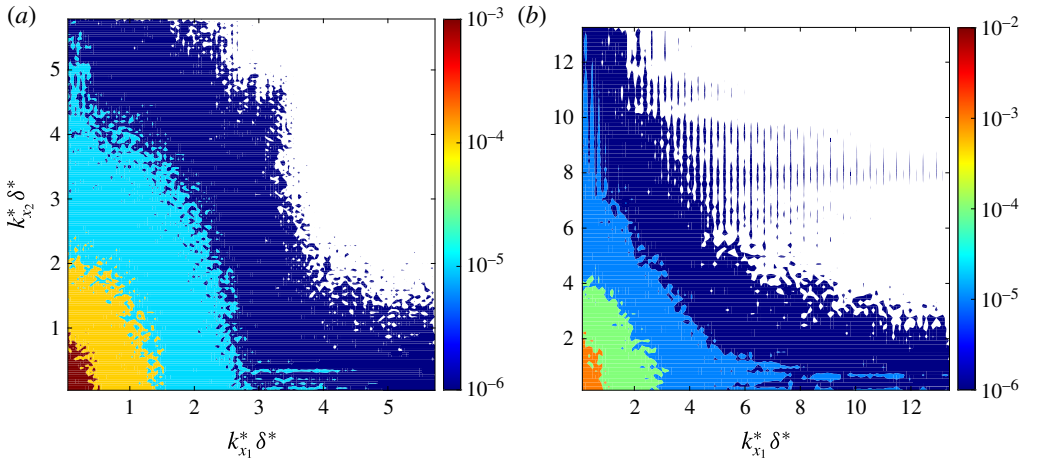


FIGURE 3. (Colour online) The 2D Fourier transform of the turbulent kinetic energy at a distance from the crests of the spheres equal to 0.0372δ. (*a*) Configuration A, $R_\delta = 400$, $t = 6.06\pi$. (*b*) Configuration B, $R_\delta = 600$, $t = 4\pi$.

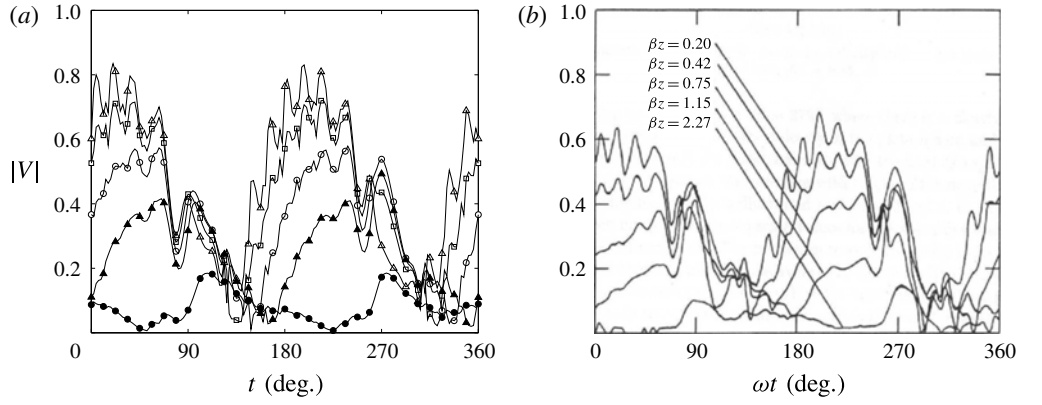


FIGURE 4. The value of $|V|$ at different distances from the crests of the spheres ($\widetilde{z}$) ($R_\delta = 95.5$, $D = 6.95$). (*a*) Numerical results with the probes at the same distances as Keiller & Sleath (1976) (–△–, $\widetilde{z} = 0.2$; –□–, $\widetilde{z} = 0.42$; –○–, $\widetilde{z} = 0.75$; –▲–, $\widetilde{z} = 1.15$; –●–, $\widetilde{z} = 2.27$). (*b*) Experimental measurements (adapted from Keiller & Sleath (1976)), $\beta z = x_3/\delta^*$.

A further relative maximum can be observed in the form of a sharp peak at a phase close to that of the inversion of the free-stream velocity.

The agreement between experimental and numerical results is fair, even though the comparison shows that the velocity computed by the code is larger than the velocity measured in the experiments. A better agreement with the experimental results of Keiller & Sleath (1976) is obtained if the distance of the numerical probes from the sphere crests is increased. Indeed, if the distance of the numerical probes is increased by $0.3\delta^*$, which corresponds to 0.53 mm, a better agreement is observed. Therefore, a small uncertainty in the position of the probes in the experiments of Keiller & Sleath (1976) could partially justify the discrepancy (see figure 4*b*).

https://doi.org/10.1017/jfm.2016.61 Published online by Cambridge University Press

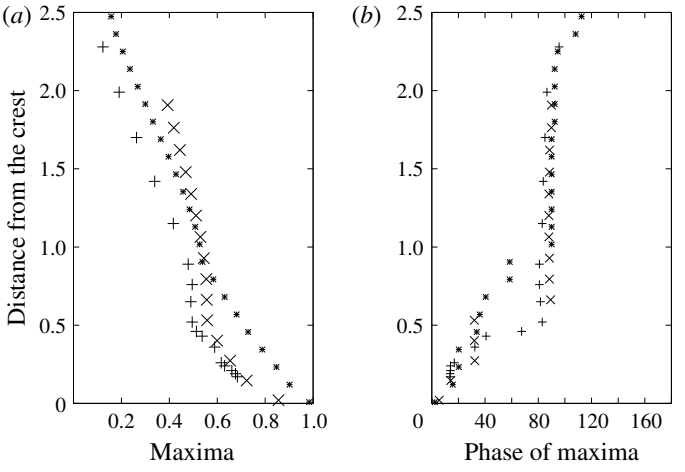


FIGURE 5. (*a*) Maxima of $|V|$ and (*b*) their phase (degrees) versus the dimensionless distance from the crests of the roughness elements $(x_3^* - x_{3c}^* - D^*/2)/\delta^*$. Symbols: *, computed values; +, measured values of Keiller & Sleath (1976); ×, numerical results of Fornarelli & Vittori (2009) ($R_\delta = 95.5, D = 6.95$).

Moreover, it is worthwhile to remind the reader of the differences between the present arrangement of the spheres and that of Keiller & Sleath (1976). Indeed, in the present simulations the spheres do not touch each other and do not touch the bottom. This small geometrical difference might also partially justify the small differences between the numerical results and the experimental measurements. An estimate of the accuracy of the present results compared with those of Ghodke *et al.* (2014) can be gained by comparing the results plotted in figure 4(*a*) of Ghodke *et al.* (2014) and the present results plotted in figure 4(*a*) with the experimental measurements of Keiller & Sleath (1976). Both the measurements of Keiller & Sleath (1976) and the present results show high-frequency oscillations, discussed previously, which are characterized by larger amplitudes during the accelerating phases. The results of Ghodke *et al.* (2014) show high-frequency oscillations of the velocity only during the decelerating phases and are absent during the accelerating phases.

A fair agreement is also found when comparing the present numerical results for the maximum of $|V|$ and the phases at which it occurs with the experimental measurements of Keiller & Sleath (1976). Figure 5 shows the present results, the measurements by Keiller & Sleath (1976) and the numerical results of Fornarelli & Vittori (2009), who considered a bed covered with half-spheres. Keiller & Sleath (1976) measured, at a distance of $0.70\delta^*$ from the crests, a maximum of the secondary peak with an amplitude equal to $0.49U_0^*$ and a relative phase of 88°. The present results show a maximum equal to $0.63U_0^*$ which is attained at a distance from the sphere crests equal to $0.68\delta^*$ at a relative phase equal to 40.5°. As discussed previously, a better agreement with experimental results is attained if the comparison is made after increasing the distance of the numerical probe from the spheres. Indeed, at a distance from the crest equal to $1.02\delta^*$, the maximum of $|V|$ is equal to 0.53 and is attained at a phase equal to 90°.

The secondary peaks of $|V|$ observed close to flow reversal were assumed to be related to the dynamics of the shear layers, which develop close to the crests of the spheres, by both Keiller & Sleath (1976) and Fornarelli & Vittori (2009).

https://doi.org/10.1017/jfm.2016.61 Published online by Cambridge University Press

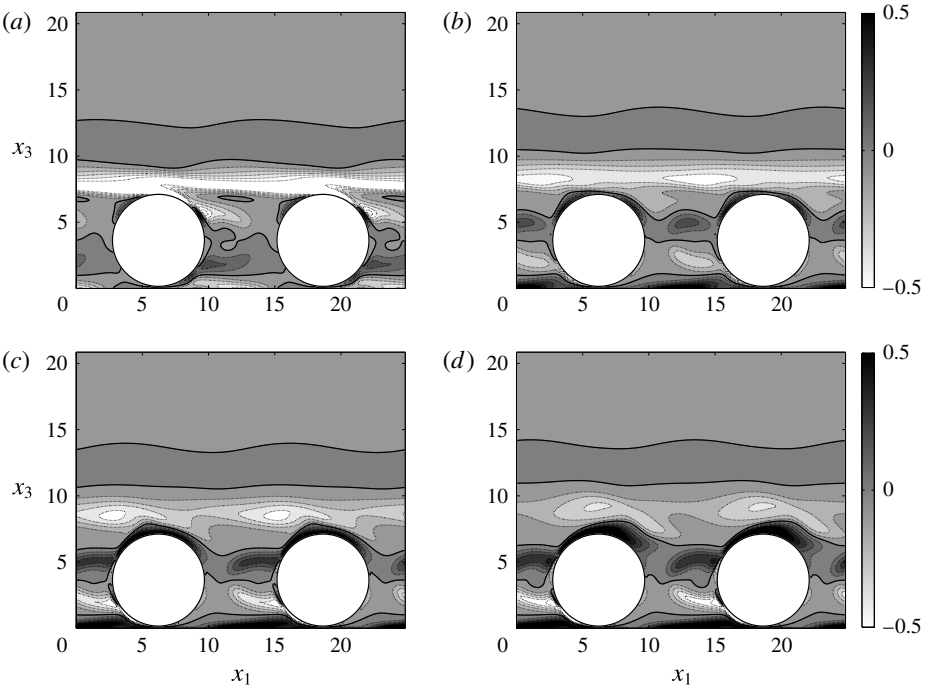


FIGURE 6. The non-dimensional spanwise vorticity component ($\Omega_2 = \Omega_2^* \delta^* / U_0^*$) on the mid plane ($x_2 = 14.35$). The thick solid line indicates vanishing values of Ω_2. The dotted curves are isovorticity curves with values of Ω_2 equispaced by 0.1. Configuration A ($D = 6.95$), $R_\delta = 95.5$; (*a*) $t = 4\pi$, (*b*) $t = 4.3\pi$, (*c*) $t = 4.4\pi$, (*d*) $t = 4.5\pi$.

Figure 6 shows the time development of the spanwise vorticity component in the mid vertical plane at different phases during the second oscillation cycle. By comparing figure 5 with figure 6 of Fornarelli & Vittori (2009) it can be noted that, notwithstanding the differences in the geometry of the roughness elements, the gross dynamics of the vorticity close to the crests is similar. It is worthwhile to point out that the sign of the spanwise vorticity is opposite to that of Fornarelli & Vittori (2009) because of the different Cartesian coordinate system used by Fornarelli & Vittori (2009).

A key point in the postprocessing of the results is the decomposition of any quantity in the average value and the fluctuating (turbulent) component. In problems where two homogeneous directions can be identified, averaged quantities can be computed by performing a 'plane average'. In the present case, the average over planes defined by $x_3 =$ constant (taking into account only the regions occupied by the fluid) is denoted by a caret. However, because of the presence of the spheres, the x_1- and x_2-directions are not strictly homogeneous directions and a more appropriate definition of averaged quantities requires the introduction of a conditional average which takes advantage of the particular geometry. In particular, the averaged value of the ith component of velocity ($\overline{u}_i$) is computed as

$$\overline{u}_i(X_1, X_2, x_3, t) = \frac{1}{N} \sum_{n=1}^{N} u_i^{(n)}(X_1, X_2, x_3, t) \phi(X_1, X_2, x_3), \tag{3.1}$$

https://doi.org/10.1017/jfm.2016.61 Published online by Cambridge University Press

D	R_δ	$\langle\widehat{E}_t\rangle$	$\langle\overline{E}_t\rangle$
6.95	95.5	0.08	2.4×10^{-11}
6.95	150	0.14	0.03
6.95	200	0.15	0.04
6.95	400	0.17	0.06
2.32	95.5	2.1×10^{-3}	1.08×10^{-15}
2.32	200	1.7×10^{-3}	1.51×10^{-15}
2.32	300	1.6×10^{-3}	2.48×10^{-15}
2.32	400	1.6×10^{-3}	4.16×10^{-13}
2.32	500	$1.8 \times 10^{-3(*)}$	$1.42 \times 10^{-8(*)}$
2.32	500	1.1×10^{-2}	4.6×10^{-3}
2.32	600	3.49×10^{-2}	1.65×10^{-2}

TABLE 2. The values of $\langle\widehat{E}_t\rangle$ and $\langle\overline{E}_t\rangle$. The values marked with (*) refer to the second oscillatory cycle (second-last cycle), while the other values are computed considering the last cycle.

where X_1, X_2 are the streamwise and spanwise coordinates with respect to a system centred on the nth sphere, N is the total number of spheres that are present in the computational domain and ϕ is a function, defined only outside the spheres, that is equal to 1 at points located inside the hexagonal prism containing the sphere and 0 otherwise. In order to increase the statistical sample, a phase-average procedure was used:

$$\bar{\bar{f}}(X_1, X_2, x_3, \varphi) = \frac{1}{N_p} \sum_{n=0}^{N_p-1} \bar{f}(X_1, X_2, x_3, t + 2\pi n) \quad \text{with } 0 \leqslant \varphi < 2\pi, \tag{3.2}$$

where N_p indicates the number of available periods.

Of course, the plane and conditional average procedures provide different values and lead to significant differences in the computed turbulence quantities. These differences are particularly relevant for moderate values of the Reynolds number and configuration A, as can be seen in table 2, which gives the time-average values $\langle\overline{E}_t\rangle$, $\langle\widehat{E}_t\rangle$ of the bulk turbulent kinetic energy of the flow, defined as

$$\langle\overline{E}_t\rangle = \frac{1}{2\pi} \int_t^{t+2\pi} \overline{E}_t \, \mathrm{d}t, \quad \langle\widehat{E}_t\rangle = \frac{1}{2\pi} \int_t^{t+2\pi} \widehat{E}_t \, \mathrm{d}t. \tag{3.3a,b}$$

The quantities $\overline{E}_t$ and $\widehat{E}_t$ are computed by volume integration of the specific turbulent kinetic energy, computed using the velocity fluctuations with respect to the conditional-averaged velocity ($\overline{e}_t$) and to the plane-averaged velocity ($\widehat{e}_t$) respectively:

$$\overline{E}_t = \frac{1}{S_h} \int \overline{e}_t \, (X_1, X_2, x_3, t) \, \mathrm{d}X_1 \, \mathrm{d}X_2 \, \mathrm{d}x_3, \quad \widehat{E}_t = \int \widehat{e}_t(x_3, t) \, \mathrm{d}x_3, \tag{3.4a,b}$$

with

$$\overline{e}_t(X_1, X_2, x_3, t) = \tfrac{1}{2} \left[\overline{(u_1 - \overline{u}_1)^2} + \overline{(u_2 - \overline{u}_2)^2} + \overline{(u_3 - \overline{u}_3)^2} \right], \tag{3.5}$$

$$\widehat{e}_t(x_3, t) = \tfrac{1}{2} \left[\widehat{(u_1 - \widehat{u}_1)^2} + \widehat{(u_2 - \widehat{u}_2)^2} + \widehat{(u_3 - \widehat{u}_3)^2} \right], \tag{3.6}$$

where S_h is the area of the base of the hexagonal prism that contains the sphere.

https://doi.org/10.1017/jfm.2016.61 Published online by Cambridge University Press

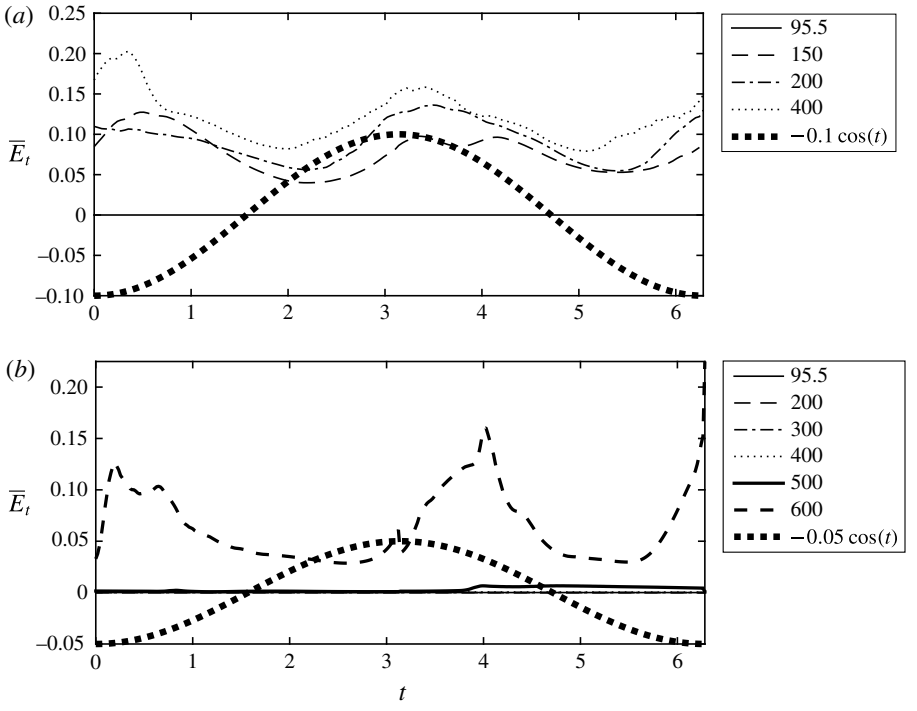


FIGURE 7. The time development of the bulk turbulent kinetic energy $\overline{E}_t$ for all of the runs performed. (*a*) Configuration A ($D = 6.95$). (*b*) Configuration B ($D = 2.32$).

If the critical conditions for transition to turbulence are determined on the basis of the turbulent kinetic energy, the use of the plane-average procedure might lead to erroneous conclusions, as can be evinced from table 2.

In the following, the fluctuating velocity components u_i' are computed as

$$u_i' = u_i - \overline{u}_i, \quad i = 1, 2, 3. \tag{3.7}$$

The high computational costs of the present simulations do not allow simulation of a large number of cycles. Although a phase-average procedure is introduced to increase the statistical sample, in many cases the averaged values are affected by the limited statistical sample. For this reason the largest part of the discussion of the results is not based on statistical quantities, which require an accurate evaluation of the mean quantities. When the discussion of the results involves averaged quantities, only qualitative conclusions are drawn.

3.2. *The flow field and vorticity dynamics*

The analysis of turbulent kinetic energy allows to identify the different flow regimes which take place as R_δ is increased.

In configuration A ($D = 6.95$), $\overline{E}_t$ is negligible throughout the cycle for $R_\delta = 95.5$ and the flow regime can be defined as laminar (see figure 7*a*). For higher values of R_δ, $\overline{E}_t$ increases during the accelerating phases and reaches its maximum value in the early decelerating phases (see figure 7*a*). The increase of the turbulent kinetic energy in configuration A is due to the presence of large vortex structures, the dynamics

https://doi.org/10.1017/jfm.2016.61 Published online by Cambridge University Press

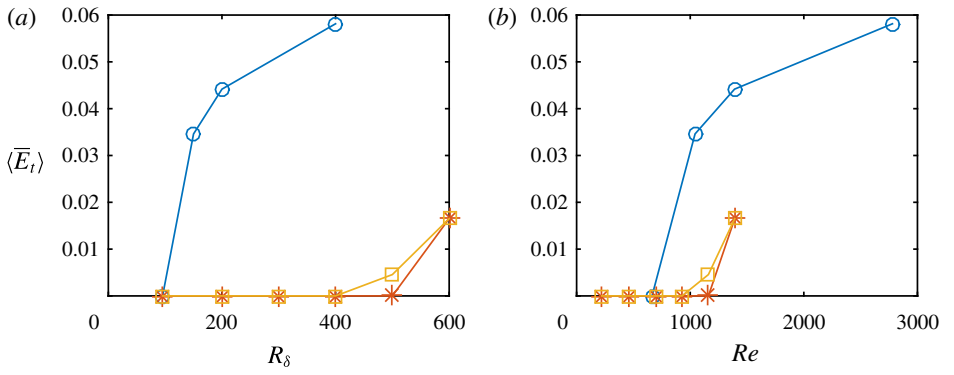


FIGURE 8. (Colour online) The time-averaged bulk turbulent kinetic energy ($\langle \overline{E}_t \rangle$) versus R_δ for all the runs performed (*a*) and versus $Re = (U_0^* D^*)/\nu^*$ (*b*): $\circ$ = configuration A ($D = 6.95$); $*$ = configuration B ($D = 2.32$) with the average computed over the second cycle; $\square$ = configuration B ($D = 2.32$) with the average computed over the third cycle.

of which differ from sphere to sphere. As time progresses, due to nonlinear effects, smaller vortex structures are formed, which induce large values of the turbulent kinetic energy. The turbulent kinetic energy during the late accelerating phases has the same order of magnitude as that characterizing the decelerating phases.

Figure 7(*b*) shows that, in configuration B ($D = 2.32$), $\overline{E}_t$ increases during the decelerating part of the cycle. Even though flow separation certainly plays a role in the transition process in configuration B, the transition process is more similar to that observed in the flat wall case by Vittori & Verzicco (1998).

Figure 8 shows the values of $\langle \overline{E}_t \rangle$ as a function both of the Reynolds numbers R_δ and $Re = (U_0^* D^*)/\nu$. In configuration A, the increase of $\langle \overline{E}_t \rangle$ with R_δ, which indicates departure from the laminar regime, takes place for R_δ ranging from 95.5 to 150 or, equivalently, for Re ranging from 664 to 1042. The results for the configuration with smaller spheres (configuration B) show non-vanishing values of $\overline{E}_t$ only for the highest value of R_δ ($R_\delta = 600$, $Re = 1392$) and during the last oscillatory cycle of the run with $R_\delta = 500$ ($Re = 1160$). As discussed in the following, the flow field for R_δ equal to 500 shows transitional characteristics, which make the values of both $\overline{E}_t$ and $\langle \overline{E}_t \rangle$ significantly different when computed during the last and second-last oscillatory cycles (see table 2 and figure 8).

Figures 7, 8 and the evolution of vorticity discussed in the following allow different flow regimes to be identified. The laminar regime is observed in configuration A only for $R_\delta = 95.5$, while in configuration B it is observed up to $R_\delta = 500$. Two turbulent regimes are identified, which are named the 'transitional turbulent regime' and the 'hydrodynamically rough turbulent regime'. The former is observed in configuration B for $R_\delta = 600$ and during the third oscillatory cycle for $R_\delta = 500$. The transitional turbulent regime is characterized by large values of the turbulent kinetic energy which are mainly confined to the decelerating phases and are related to the formation of small turbulent eddies. These turbulent eddies are generated by the intrinsic instability of the oscillatory Stokes flow with a small contribution from the bottom roughness. The hydrodynamically rough turbulent regime, which is characterized by fluctuations that appear to be more influenced by the presence of the roughness than by a mere instability process, is observed only in configuration A and for values of the Reynolds number larger than 100.

https://doi.org/10.1017/jfm.2016.61 Published online by Cambridge University Press

R_δ	D	$\max(\lvert\Omega_1^*\delta^*/U_0^*\rvert)$	$\max(\lvert\Omega_2^*\delta^*/U_0^*\rvert)$	$\max(\lvert\Omega_3^*\delta^*/U_0^*\rvert)$
95.5	6.95	1.49	4.46	1.98
150	6.95	3.16	5.16	3.41
200	6.95	4.62	5.73	4.70
400	6.95	6.70	7.31	6.87
95.5	2.32	0.55	3.04	1.17
200	2.32	0.72	3.21	1.24
300	2.32	0.83	3.13	1.35
400	2.32	0.96	3.05	1.52
500	2.32	$1.16^{(*)}$	$3.26^{(*)}$	$1.77^{(*)}$
500	2.32	4.57	5.79	4.42
600	2.32	9.50	13.93	10.28

TABLE 3. The maximum values of the dimensionless vorticity components computed over the last oscillatory cycle. The values marked with (*) refer to the second oscillatory cycle.

In the following, the conclusions derived on the basis of the analysis of the turbulent kinetic energy will be confirmed by the analysis of the vorticity fields and of the forces exerted on the spheres.

In all of the runs, the maximum of the spanwise component of the vorticity (Ω_2) is larger than the maxima of the streamwise and cross-stream components (see table 3). The maximum of the cross-stream component of vorticity (Ω_3) is larger than the maximum of the streamwise component and, as the Reynolds number is increased, the three components of the vorticity tend to assume comparable values. For the same value of R_δ, the maximum values attained by Ω_1 and Ω_3 for configuration A are larger than the corresponding values for configuration B. This indicates that the runs for configuration B are characterized by smaller convective effects than configuration A.

The time development of the spanwise component of the vorticity Ω_2, plotted in figures 9 and 10, shows that Ω_2 is generated at the sphere crests during the accelerating phases of the cycle and is associated with the formation of shear layers. In configuration A and for the lower values of R_δ (see figure 9), when the flow falls in the laminar regime, long streaks of vorticity, characterized by values of Ω_2 of the same sign, form immediately above the sphere crests when the flow accelerates. These streaks eventually lift from the bottom, dissipate and reform with vorticity of opposite sign during the following half-cycle. For larger values of R_δ, so that the flow falls in the hydrodynamically rough turbulent regime, regular long streaks of spanwise vorticity cannot be recognized. Indeed, shortly after the formation of the spanwise vorticity at the crests, the regions with high values of Ω_2 elongate in the flow direction, interact with the crest of the following spheres, break and lift from the bottom. Small regions of vorticity of opposite sign are observed at the end of the accelerating phase, when the vorticity shed from the crests breaks up into small vortex structures.

In configuration B, the vorticity field shows a clear spatial and temporal periodicity up to $R_\delta = 500$. For $R_\delta = 600$, towards the late accelerating and early decelerating phases, the spanwise vorticity, released from the top of the spheres, forms streaks elongated in the streamwise direction (see figure 10) which then break into small eddies and turbulence appears.

The cross-stream component of vorticity Ω_3 is first generated at the sides of the spheres and, as time progresses, is convected downstream. In configuration A,

https://doi.org/10.1017/jfm.2016.61 Published online by Cambridge University Press

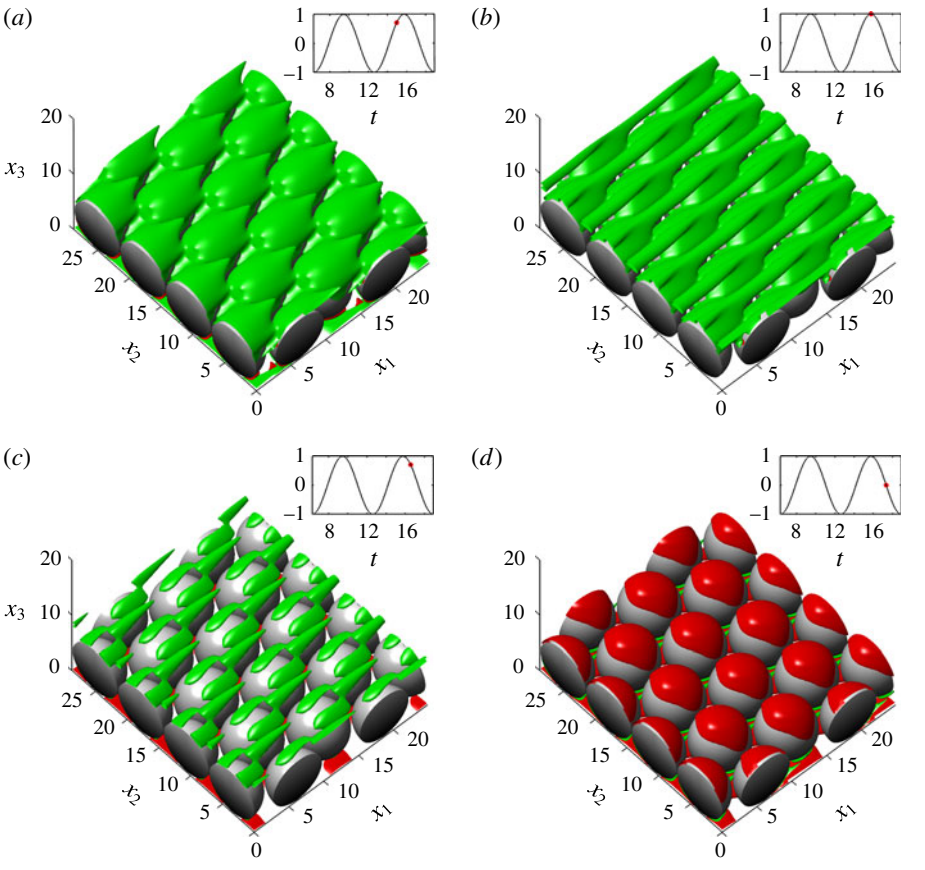


FIGURE 9. (Colour online) Isocontours of the dimensionless spanwise component of vorticity ($\Omega_2 = \Omega_2^* \delta^*/U_0^*$), $\Omega_2 = \pm 0.446$. Light grey (green online) = positive vorticity, dark grey (red online) = negative vorticity; $R_\delta = 95.5$. Configuration A ($D = 6.95$): (*a*) $t = 0.75\pi$, (*b*) $t = \pi$, (*c*) $t = 1.25\pi$, (*d*) $t = 1.5\pi$.

the convection of Ω_3 causes the formation of streaks of cross-stream vorticity of alternating sign (see figure 11). The presence of bands of cross-stream vorticity of alternate sign suggests the formation of low- and high-speed streaks in the region immediately above the crests. The streaks dissipate during the decelerating phase and a specular flow field is generated when the free-stream flow reverses. As the Reynolds number is increased, the streaks of cross-stream vorticity (Ω_3) become more irregular, lift from the crests of the spheres, due to their interaction with the following spheres, break up and dissipate more quickly than the cases at lower values of R_δ. In configuration B, the convection of cross-stream vorticity by the mean flow is weaker and no streaks are observed for values of the Reynolds number up to 500. For $R_\delta = 600$ (see figure 12), when the flow falls in the transitional regime, streaks are observed during the late acceleration and early decelerating phases. Then, as the flow decelerates, the streaks break up and vorticity is ejected far from the wall. A similar evolution was observed by Costamagna *et al.* (2003), who reported the formation of ejection events in the oscillatory boundary layer over a smooth wall.

The streamwise component of the vorticity Ω_1, for both configurations A and B, is similar to that of Ω_3. In configuration A, Ω_1 is generated during the decelerating

https://doi.org/10.1017/jfm.2016.61 Published online by Cambridge University Press

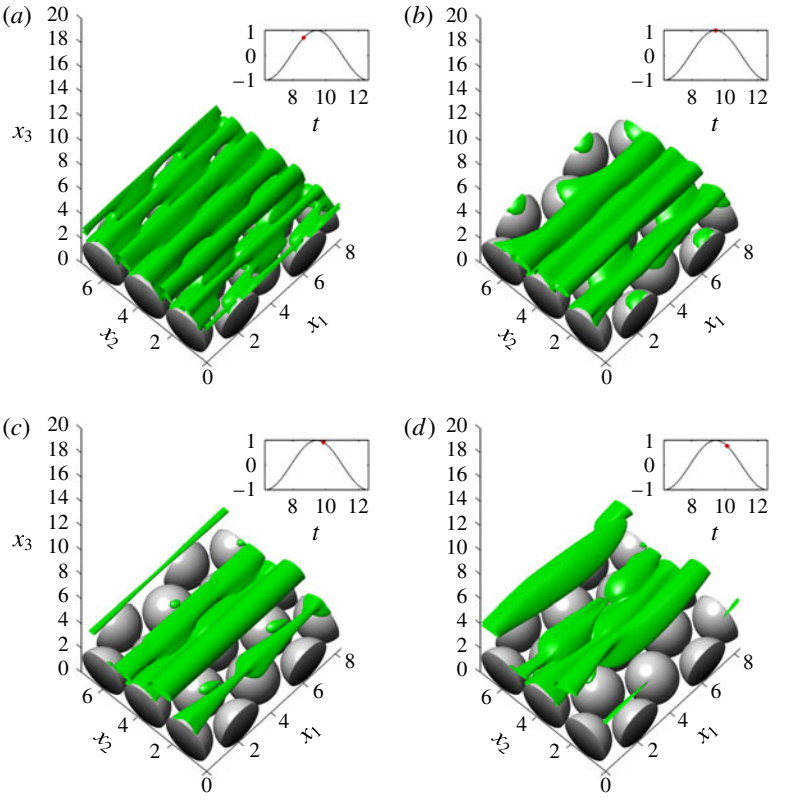


FIGURE 10. (Colour online) Isocontours of the dimensionless spanwise component of vorticity ($\Omega_2 = \Omega_2^* \delta^*/U_0^*$), $\Omega_2 = \pm 0.70$. Light grey (green online) = positive vorticity, dark grey (red online) = negative vorticity; $R_\delta = 600$. Configuration B ($D = 2.32$): (*a*) $t = 0.75\pi$, (*b*) $t = \pi$, (*c*) $t = 1.13\pi$, (*d*) $t = 1.22\pi$.

phases at the sides of the spheres and builds up during the accelerating phases. The regions of high values of Ω_1 are convected by the mean flow and the value of Ω_1 increases due to the stretching of vorticity by the flow. During the decelerating phases the vortex structures are rapidly dissipated.

In configuration B and for $R_\delta = 600$, the regions with high values of Ω_1 organize into streaks which eventually break up and are ejected far from the wall.

In configuration B and for $R_\delta = 500$, the flow shows peculiar characteristics. Indeed, the evolution of vorticity during the second oscillatory cycle is similar to that observed for lower values of R_δ. Then, during the second decelerating phase of the third oscillatory cycle, large disturbances, similar to Tollmien–Schlichting waves, appear. The vorticity released from the crests of the spheres is subject to oscillations with a clear streamwise and temporal periodicity (see figure 13 and supplementary movie 1 available at http://dx.doi.org/10.1017/jfm.2016.61). As time progresses, the amplitude of the oscillations increases and eventually the large coherent vortex structures break, generating small eddies which later dissipate. The whole process takes place over a limited time interval during the decelerating phase, precisely for t ranging from 5π to 5.33π. The quantity λ_2, introduced by Jeong & Hussain (1995) to detect coherent vortex structures, shows that when the large disturbances appear

https://doi.org/10.1017/jfm.2016.61 Published online by Cambridge University Press

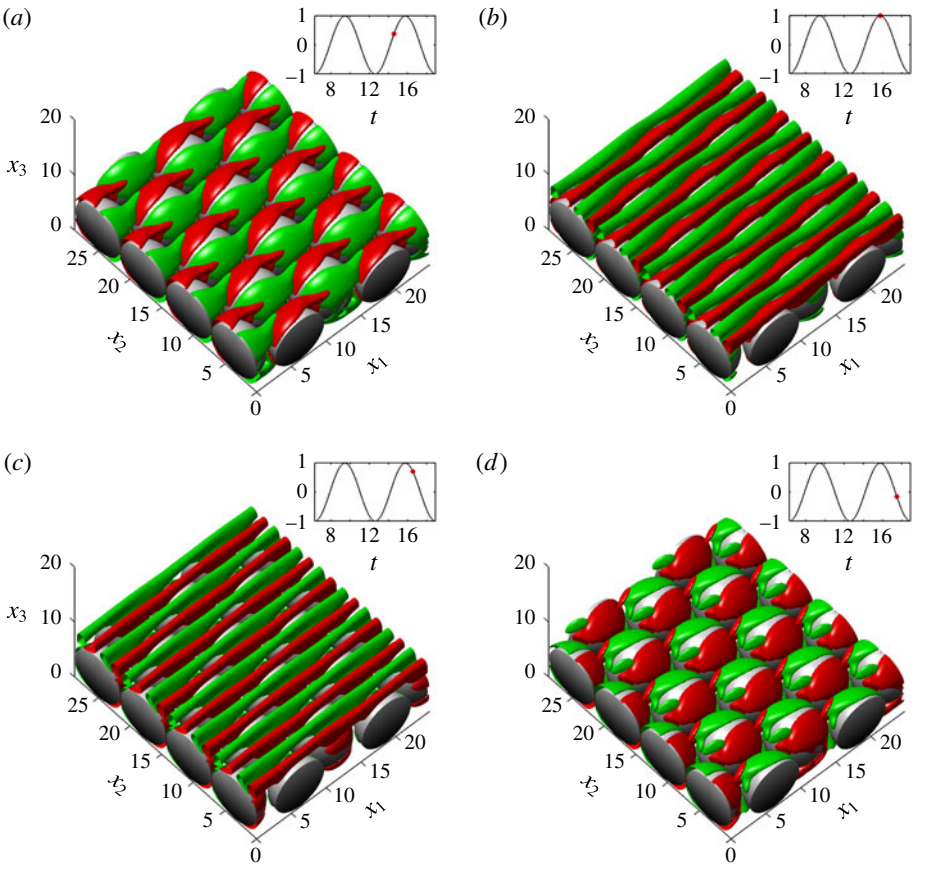


FIGURE 11. (Colour online) Isocontours of the dimensionless cross-stream component of vorticity ($\Omega_3 = \Omega_3^* \delta^*/U_0^*$), $\Omega_3 = \pm 0.20$. Light grey (green online) = positive vorticity, dark grey (red online) = negative vorticity; $R_\delta = 95.5$. Configuration A ($D = 6.95$): (*a*) $t = 0.63\pi$, (*b*) $t = \pi$, (*c*) $t = 1.25\pi$, (*d*) $t = 1.55\pi$.

for $R_\delta = 500$, horseshoe vortices form upstream of the spheres while the structures released from the crests generate hairpin vortices (see figure 14 and supplementary movie 1). A similar pattern of coherent structures was observed around isolated hemispherical roughness elements in steady boundary layers by Acarlar & Smith (1987) and Zhou, Wang & Fan (2010).

3.3. *Hydrodynamic force on the spheres*

Knowledge of the velocity and pressure fields allows evaluation of the strain rate tensor, the viscous stresses and the force acting on the roughness elements. In the two turbulent regimes previously identified, the force shows a dependence on the sphere considered, due to the random variations of the vortex structures and the subsequent formation of smaller vortices characterized by a random spatial distribution. In order to provide information on the general characteristics of the force exerted on the roughness elements, the force averaged over all of the spheres ($\overline{F}_{x1}$, $\overline{F}_{x2}$, $\overline{F}_{x3}$) is

https://doi.org/10.1017/jfm.2016.61 Published online by Cambridge University Press

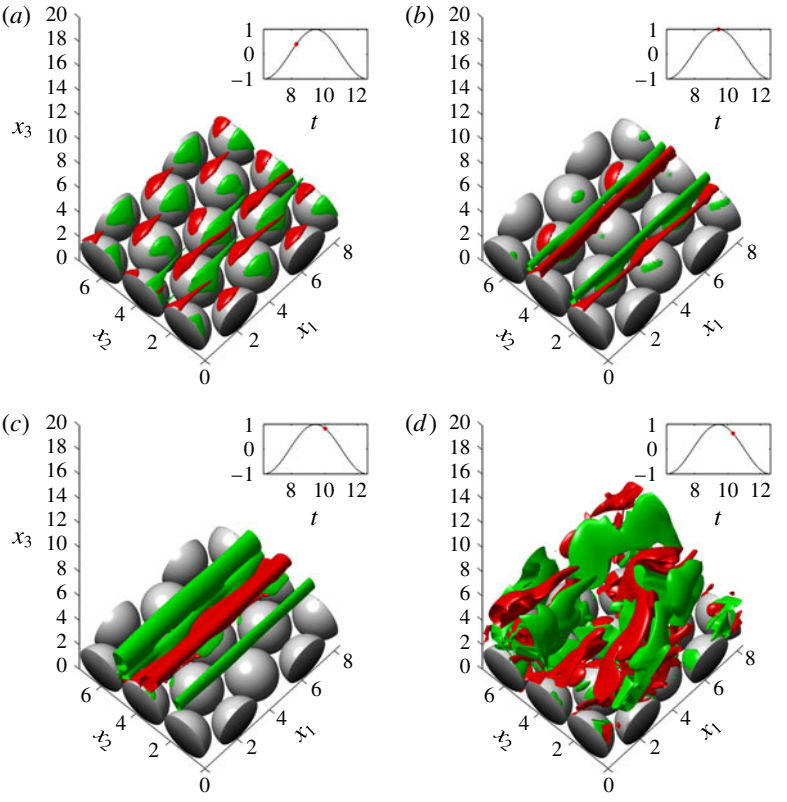


FIGURE 12. (Colour online) Isocontours of the dimensionless cross-stream component of vorticity ($\Omega_3 = \Omega_3^*\delta^*/U_0^*$), $\Omega_3 = \pm 0.515$. Light grey (green online) = positive vorticity, dark grey (red online) = negative vorticity; $R_\delta = 600$. Configuration B ($D = 2.32$): (*a*) $t = 0.63\pi$, (*b*) $t = \pi$, (*c*) $t = 1.19\pi$, (*d*) $t = 1.29\pi$.

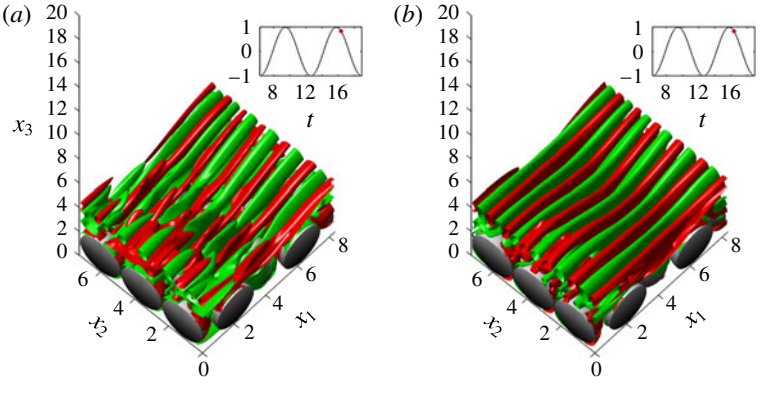


FIGURE 13. (Colour online) Isocontours of the dimensionless (*a*) streamwise ($|\Omega_1| = \pm 0.116$) and (*b*) cross-stream ($|\Omega_3| = \pm 0.177$) components of vorticity at $t = 5.19\pi$; $R_\delta = 500$, configuration B ($D = 2.32$): light grey (green online) = positive vorticity, dark grey (red online) = negative vorticity.

https://doi.org/10.1017/jfm.2016.61 Published online by Cambridge University Press

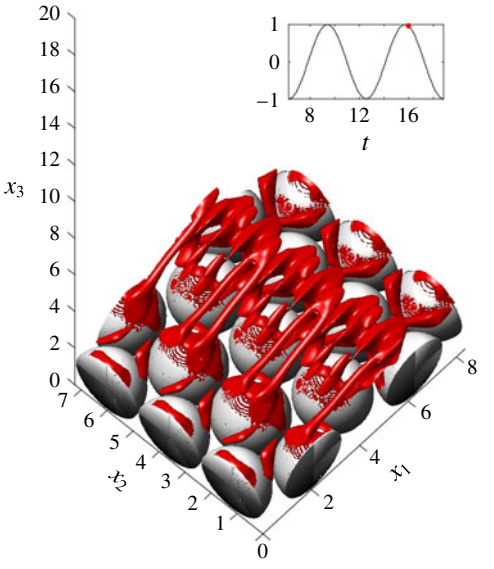


FIGURE 14. (Colour online) Isosurfaces of λ_2 ($\lambda_2 = -0.11$); $R_\delta = 500$, $t = 5.08\pi$, configuration B ($D = 2.32$).

presented. The force averaged over all spheres is decomposed into a contribution related to pressure $(\overline{F}_{x1}^{(p)}, \overline{F}_{x2}^{(p)}, \overline{F}_{x3}^{(p)})$ and a contribution related to viscous stresses $(\overline{F}_{x1}^{(v)}, \overline{F}_{x2}^{(v)}, \overline{F}_{x3}^{(v)})$:

$$(\overline{F}_{x1}^{(p)}, \overline{F}_{x2}^{(p)}, \overline{F}_{x3}^{(p)}) = \int_S (-\overline{p} n_{x1}, -\overline{p} n_{x2}, -\overline{p}\ n_{x3})\, \mathrm{d}S, \tag{3.8}$$

$$(\overline{F}_{x1}^{(v)}, \overline{F}_{x2}^{(v)}, \overline{F}_{x3}^{(v)}) = \int_S \left[(\bar{t}_{x1}, \bar{t}_{x2}, \bar{t}_{x3}) + (\overline{p}\ n_{x1}, \overline{p}\ n_{x2}, \overline{p}\ n_{x3})\right] \mathrm{d}S, \tag{3.9}$$

where (n_{x1}, n_{x2}, n_{x3}) is the unit vector orthogonal to the surface S of the sphere and $(\bar{t}_{x1}, \bar{t}_{x2}, \bar{t}_{x3})$ is the average (dimensionless) stress exerted by the fluid on S, which is scaled as the pressure. The force components are made dimensionless using the quantity $\rho^* U_0^{*2} \delta^{*2}$.

Figure 15 shows the streamwise and cross-stream force components, along with the corresponding components computed by Fornarelli & Vittori (2009). In the same figure, the viscous and pressure contributions are also shown in (*b*) and (*c*) respectively. The streamwise component of the force of the present study has a time development similar to that computed by Fornarelli & Vittori (2009), even though its maximum value lags ahead of that evaluated by Fornarelli & Vittori (2009). Indeed, both the viscous and pressure contributions show a maximum that takes place before that evaluated by Fornarelli & Vittori (2009). As discussed later, this difference is due to the force exerted by the fluid on the lower half of the surface of the spheres, which is not present in the computations of Fornarelli & Vittori (2009).

The cross-stream component of the force is characterized by a time development grossly similar to that observed by Fornarelli & Vittori (2009). However, the present results show clearly the presence of a secondary peak close to flow reversal, which is related to the formation of areas of positive pressure on the lower downstream

https://doi.org/10.1017/jfm.2016.61 Published online by Cambridge University Press

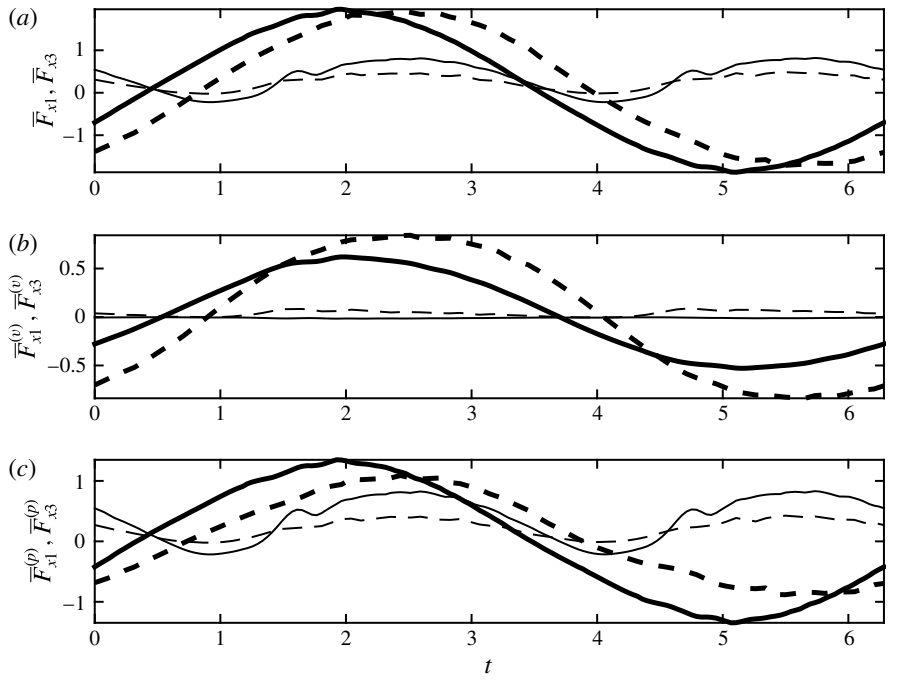


FIGURE 15. The time development of the averaged streamwise and cross-stream components of the force (*a*) exerted on the spherical roughness element, of its viscous component (*b*) and of its pressure component (*c*). Thick lines = streamwise component, thin lines = cross-stream component; present geometry = solid lines, Fornarelli & Vittori (2009) = broken lines. All quantities are made non-dimensional by means of $\rho U_0^{*2}\delta^{*2}$.

surface of the spheres, as discussed in the following. Moreover, differently from Fornarelli & Vittori (2009), during the decelerating phases of the cycle, the present results show negative values of the cross-stream component of the force. A lift force directed towards the wall has also been observed by Rosenthal & Sleath (1986), who measured the lift force on an isolated sphere close to a wall in an oscillatory boundary layer. This effect appears to be related to the anticipated flow reversal near the wall, which causes the formation of areas of negative pressure on the lower surface of the spheres.

The viscous contribution to the cross-stream force is much smaller than the pressure contribution both for present results and for those of Fornarelli & Vittori (2009).

The comparison of the present results with those of Fornarelli & Vittori (2009), who considered half-spheres as roughness elements, shows that the details of the geometry of the roughness elements have a small influence on the velocity field above the roughness elements (see the previous section), but have a significant effect on the force, because the lower part of the sphere surface contributes significantly to the total force.

The time development of the averaged force components is plotted in figures 16 and 17 for all of the Reynolds numbers presently simulated and for configurations A and B respectively. The spanwise component of the force, as expected, turns out to be negligible and it is not shown in figures 16 and 17.

Often, for practical purposes, the streamwise component of the force is decomposed into a part proportional to the external velocity and a part proportional to the external

https://doi.org/10.1017/jfm.2016.61 Published online by Cambridge University Press

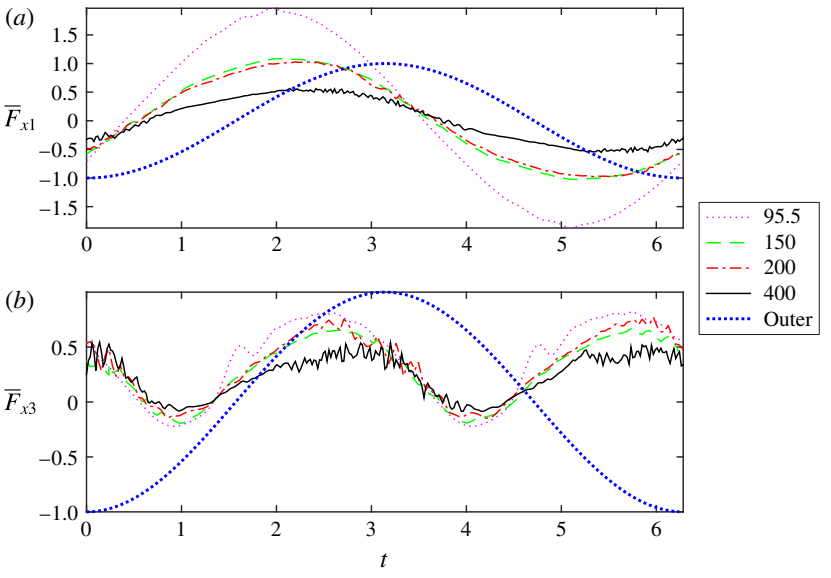


FIGURE 16. (Colour online) The time development of the streamwise (*a*) and cross-stream (*b*) components of the dimensionless force ($\overline{F} = \overline{F}^*/(\rho U_0^{*2}\delta^{*2})$), averaged over all of the spheres, for all of the considered values of R_δ and for configuration A ($D = 6.95$). The thick-dotted line (blue online) indicates the time development of the velocity outside the boundary layer.

R_δ	D	$\bar{\bar{F}}_x^{(s)}$	$\bar{\bar{F}}_x^{(w)}$
95.5	6.95	16.97	3.41
150	6.95	10.11	2.09
200	6.95	9.48	1.48
400	6.95	5.54	0.73
95.5	2.32	10.67	0.26
200	2.32	5.29	0.12
300	2.32	3.62	0.08
400	2.32	2.78	0.06
500	2.32	1.12	0.02
600	2.32	1.11	0.02

TABLE 4. The drag force on the spheres ($\bar{\bar{F}}_x^{(s)}$) and on the plane wall ($\bar{\bar{F}}_x^{(w)}$), averaged over the half-oscillation-period.

acceleration. The present results show that the latter contribution prevails over the former.

Table 4 shows the module of the drag exerted by the fluid on the spheres ($\bar{\bar{F}}_x^{(s)}$) and on the plane wall ($\bar{\bar{F}}_x^{(w)}$), averaged over the half-oscillation-period during which the free-stream velocity is either positive or negative.

The cross-stream component of the force ($\overline{F}_{x3}$) is mainly related to the effect of pressure and attains its maximum value later than $\overline{F}_{x1}$. In configuration A and for $R_\delta = 95.5$, $\overline{F}_{x3}$ shows a secondary peak close to flow reversal (see figure 16), which

https://doi.org/10.1017/jfm.2016.61 Published online by Cambridge University Press

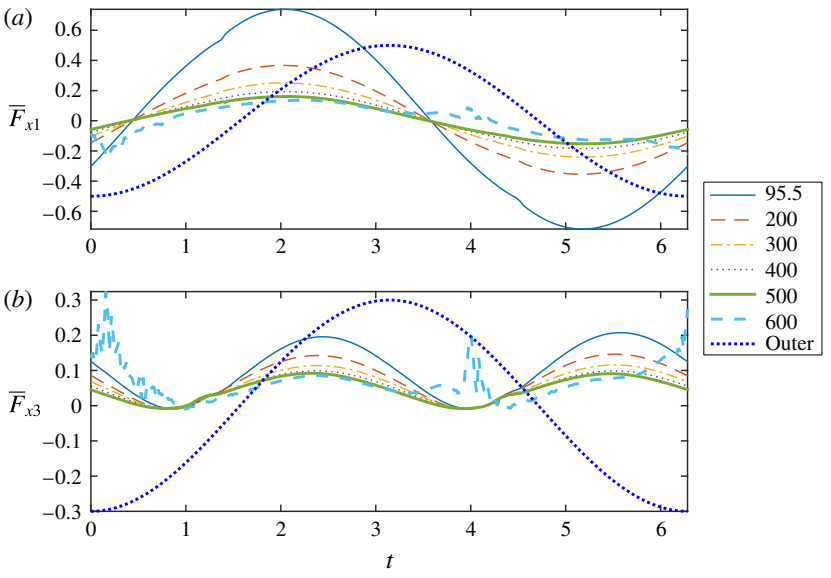


FIGURE 17. (Colour online) The time development of the streamwise (*a*) and cross-stream (*b*) components of the dimensionless force ($\overline{F} = \overline{F}^*/(\rho U_0^{*2}\delta^{*2})$), averaged over all of the spheres, for all of the considered values of R_δ and for configuration B ($D = 2.32$). The thick-dotted line (blue online) indicates the time development of the velocity outside the boundary layer.

has been discussed previously. For higher values of R_δ, as well as for configuration B, no secondary maximum is observed because the regions of positive pressure located in the lower part of the spheres are of similar extension and intensity to those located in the upper part of the spheres. Prior to flow reversal, negative values of the vertical force are observed, which are more evident for configuration A (see figure 16*b*). In configuration B for $R_\delta = 600$, when the flow is in the transitional turbulent regime, at the end of the decelerating phases a significant increase of the streamwise force component and large values of the vertical force component can be observed. As discussed below, in this flow regime the force experienced by each sphere might be significantly different. Therefore, the increase of the mean vertical force on the spheres suggests that some spheres might be picked up from the bottom during these phases, if free to move.

3.3.1. *Contribution of pressure and viscous stresses to the force*

The contribution of pressure and viscous stresses to the force exerted on the roughness elements is different for the two bottom configurations presently considered. In configuration A, the pressure contribution to the streamwise component of the force is larger than the viscous contribution for all of the simulated Reynolds numbers, as can be seen in figure 18, which shows the pressure and viscous contribution to the force for $R_\delta = 400$.

In configuration B, the two contributions contribute equally to the streamwise force (see figure 19*a*). The viscous contribution to the cross-stream force component ($\overline{F}_{x3}$) is negligible for both bottom configurations A and B and for all of the values of R_δ (see figures 18*b* and 19*b*). Therefore, the lift force on the spheres is mainly related to the

https://doi.org/10.1017/jfm.2016.61 Published online by Cambridge University Press

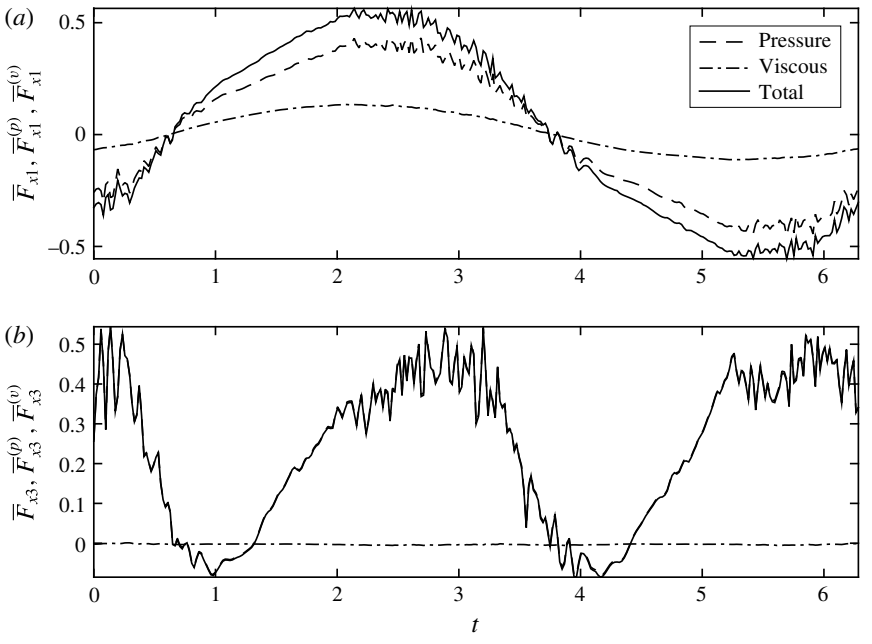


FIGURE 18. The time development of the different contributions to the average dimensionless force components for configuration A ($D = 6.95$), $R_\delta = 400$.

effect of pressure and reaches its maximum value before that of the outer flow, mainly due to the formation, at the end of the accelerating phases, of regions of negative pressure at the crests of the spheres, related to the formation of free shear layers.

The analysis of the averaged pressure on the sphere surface at different phases during the oscillatory cycle shows that during the accelerating parts of the cycle, when a free shear layer is shed from the crest of the sphere, pressure is minimum at the top of the sphere and two areas of positive pressure form on the upstream part of the sphere surface (see figure 20*a*). It is worthwhile to point out that figures 20–22 show averaged quantities. Therefore, the sphere appearing in figures 20–22 is not a particular sphere of the configuration considered.

The first positive pressure area is located close to the crest while the second one is located close to the bottom. Considering the vortex structures, which are shed by the spheres, it appears that the upper area of positive pressure is related to the impact of the shear layers released from the upstream sphere. Later, during the decelerating phases, the strength of the shear layers decreases and the vortex structures released from the upstream spheres are deflected. As a consequence, the positive pressure region close to the top appears more elongated towards the sides of the sphere while the positive pressure area close to the bottom decreases and eventually disappears, due to the flow reversal taking place close to the bottom (see figure 20*b*). At the later stages of the decelerating cycle, due to near-bed flow reversal, areas of positive pressure appear on the downstream part of the sphere surface while a region of negative pressure forms at the bottom of the sphere (see figure 20*c*). The main differences in the time development of pressure on the surface of the spheres in the two configurations appear to be related to the small sphere diameter in configuration B. Indeed, near the plane wall, flow reversal takes place earlier than far from it and

https://doi.org/10.1017/jfm.2016.61 Published online by Cambridge University Press

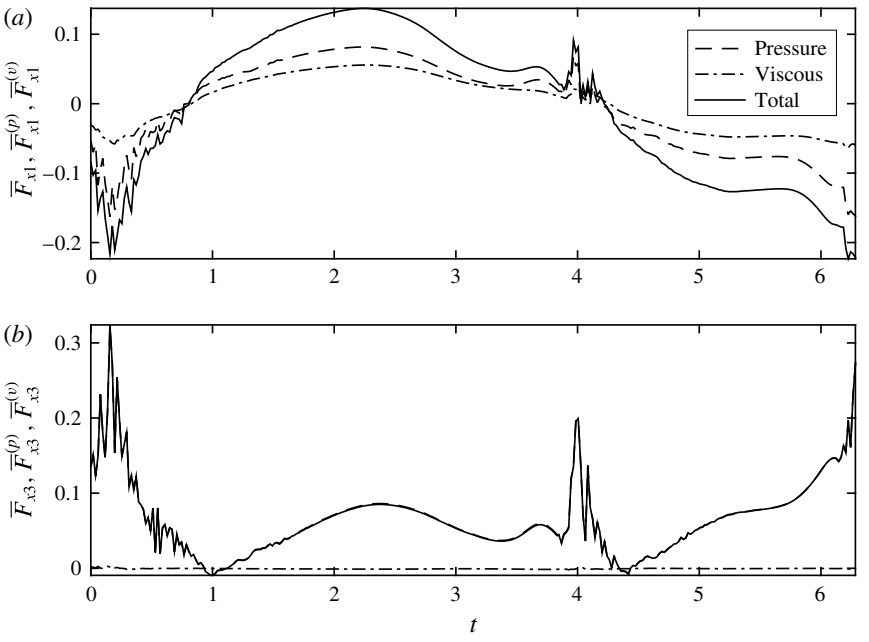


FIGURE 19. The time development of the different contributions to the average dimensionless force components for configuration B ($D = 2.32$), $R_\delta = 600$.

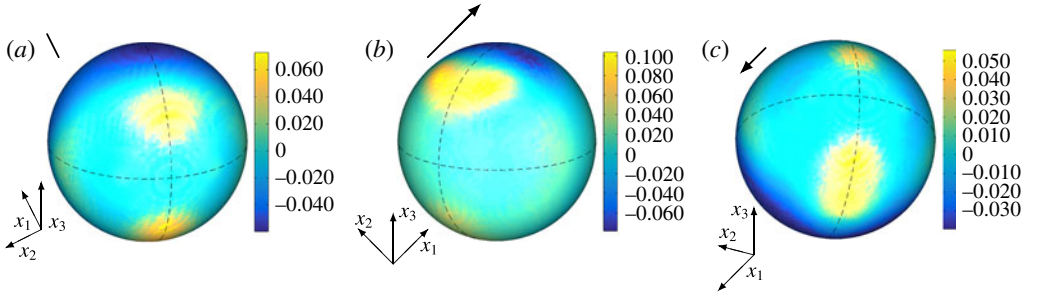


FIGURE 20. (Colour online) The dimensionless averaged pressure exerted on the spherical roughness element. Configuration A ($D = 6.95$), $R_\delta = 95.5$: (*a*) $t = 2.5\pi$, (*b*) $t = 2.9\pi$, (*c*) $t = 3.4\pi$.

the evolution of pressure on the surface of the roughness element in configuration B is anticipated with respect to that of configuration A. Moreover, the proximity to the wall of the smaller spheres means that the flow around the spheres is more affected by the vorticity generated at the plane wall. As a consequence, diffuse regions of positive pressure are observed on the upstream surface of the sphere as the flow accelerates (see figure 21*a*). For $R_\delta = 600$ the effect of turbulent fluctuations, confined to the decelerating phases, counteracts the near-wall flow reversal and, differently from the laminar flow regime, the upstream part of the sphere surface is subject to positive pressure for most of the decelerating part of the cycle (see figure 21*b*). It is only at flow reversal that regions of positive pressure are observed on the downstream part of the sphere surface (see figure 21*d*). The reader will notice that in figures 20 and

https://doi.org/10.1017/jfm.2016.61 Published online by Cambridge University Press

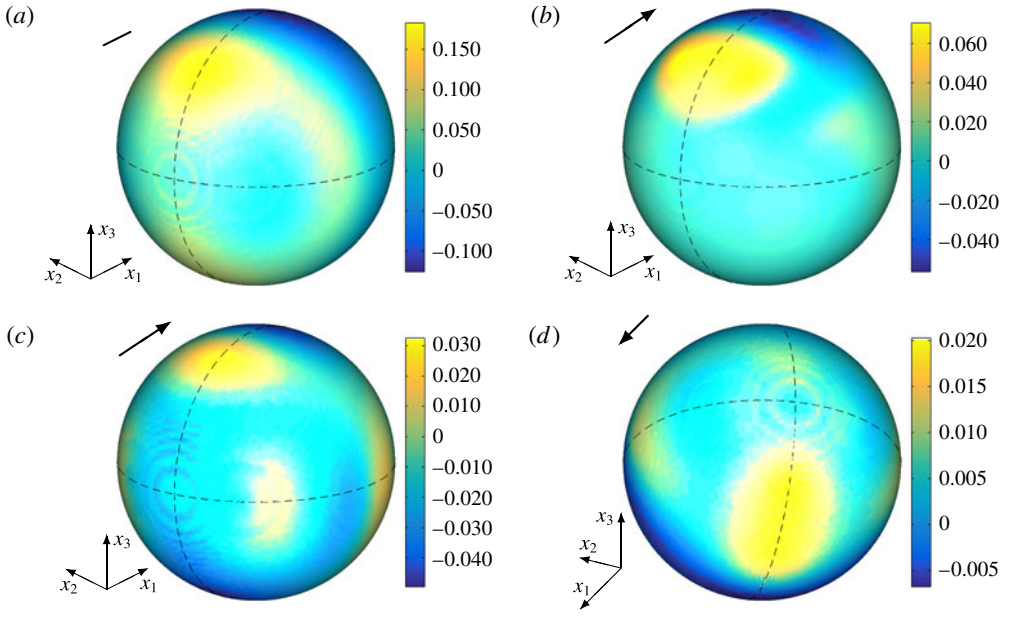


FIGURE 21. (Colour online) The dimensionless averaged pressure exerted on the spherical roughness element. Configuration B ($D = 2.32$): (*a*,*c*) $R_\delta = 95.5$, (*a*) $t = 2.5\pi$, (*c*) $t = 3.4\pi$; (*b*,*d*) $R_\delta = 600$, (*b*) $t = 3.2\pi$, (*d*) $t = 3.4\pi$.

21 some oscillations appear. These oscillations are not physically significant as they are due to the direct forcing used in the immersed boundary method.

The analysis of the average force exerted on the spheres shows that viscous stresses influence only the streamwise component of the force. For this reason, only the streamwise component of the viscous stress on the surface of the sphere is discussed. Similarly to the pressure, the time development of the streamwise component of the viscous stress appears to be strongly influenced by the shear layers that form at and are released from the surface of the spheres. Indeed, when the external flow accelerates and the shear layers form, on the top of the sphere a region of high viscous stress, with the same sign as the free-stream velocity, is observed (see the areas with positive values in figure 22*a–c*). As the external velocity increases, the intensity of the stresses at the top of the sphere increases, too. Prior to flow reversal, due to near-bed flow reversal, regions of stress with opposite sign form on the part of the sphere surface closer to the bottom (see the areas with negative values in figure 22*d–f*). In configuration B, as already mentioned, the effects of near-bed flow reversal appear earlier, and regions of negative stress are observed before the end of the decelerating phase.

3.3.2. *Spatial variability of the force*

As previously mentioned, when turbulent fluctuations appear, the value of the force exerted by the fluid over each sphere takes different values. On the other hand, in the laminar regime (see figure 23), at each instant the force exerted on each sphere has the same value and shows a clear periodicity in time.

Figures 24 and 25 show the root mean square (r.m.s.) values of the three components of the force for configurations A and B respectively. It can be seen

https://doi.org/10.1017/jfm.2016.61 Published online by Cambridge University Press

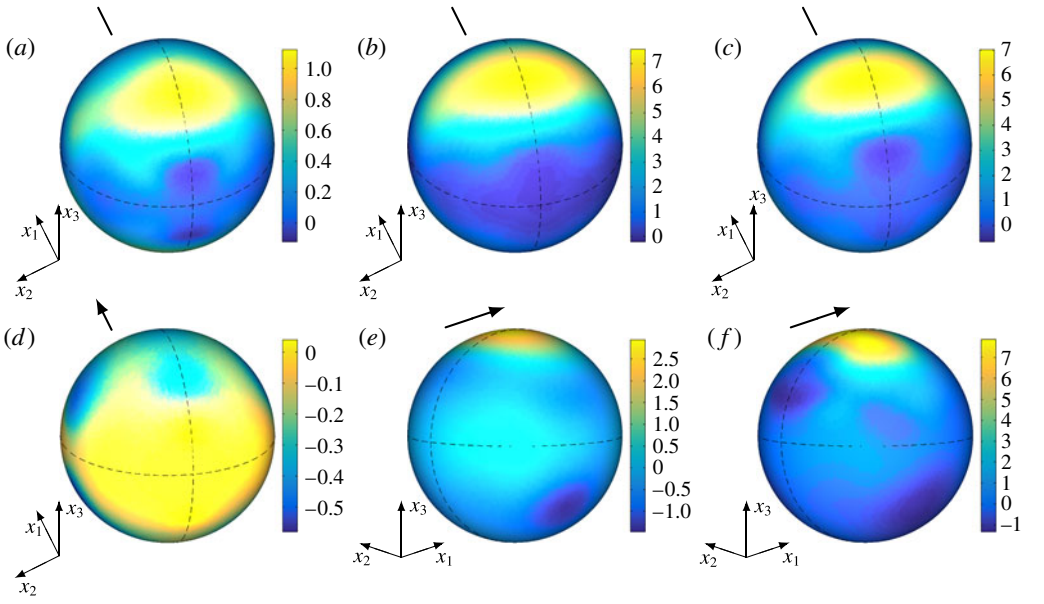


FIGURE 22. (Colour online) The dimensionless averaged streamwise component of the viscous stress exerted on the spherical roughness element. (*a*,*d*) Configuration A ($D = 6.95$), $R_\delta = 95.5$, (*a*) $t = 2.5\pi$, (*d*) $t = 3.4\pi$; (*b*,*e*) configuration B ($D = 2.32$), $R_\delta = 95.5$, (*b*) $t = 2.5\pi$, (*e*) $t = 3.2\pi$; (*c*,*f*) configuration B ($D = 2.32$), $R_\delta = 600$, (*c*) $t = 2.7\pi$, (*f*) $t = 3.2\pi$.

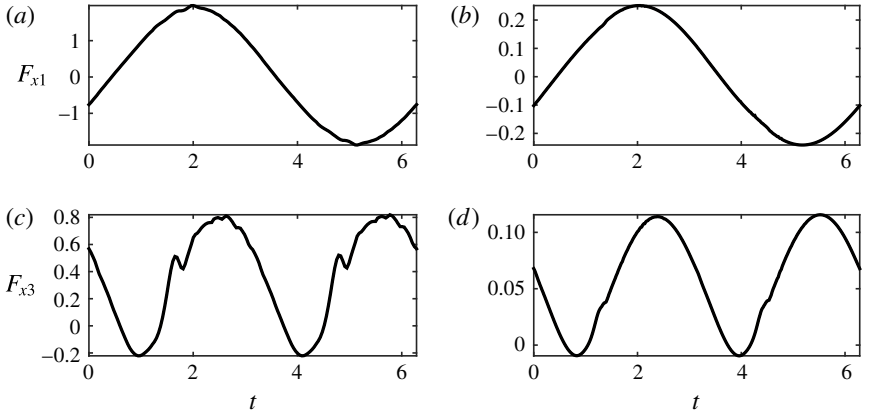


FIGURE 23. The force components on each sphere for configuration A ($D = 6.95$) and $R_\delta = 95.5$ (*a*,*c*) and for configuration B ($D = 2.32$) and $R_\delta = 300$ (*b*,*d*). The curves for the different spheres are indistinguishable from the average value (thick line).

that in the cases when the flow is in the laminar regime, the r.m.s. values of the force components vanish. For the highest values of the Reynolds number, when the flow is in any of the two turbulent regimes previously identified, the r.m.s. of the force attains non-vanishing values since the force at each phase shows a variability from one sphere to another. In particular, differences in the force measured on each

https://doi.org/10.1017/jfm.2016.61 Published online by Cambridge University Press

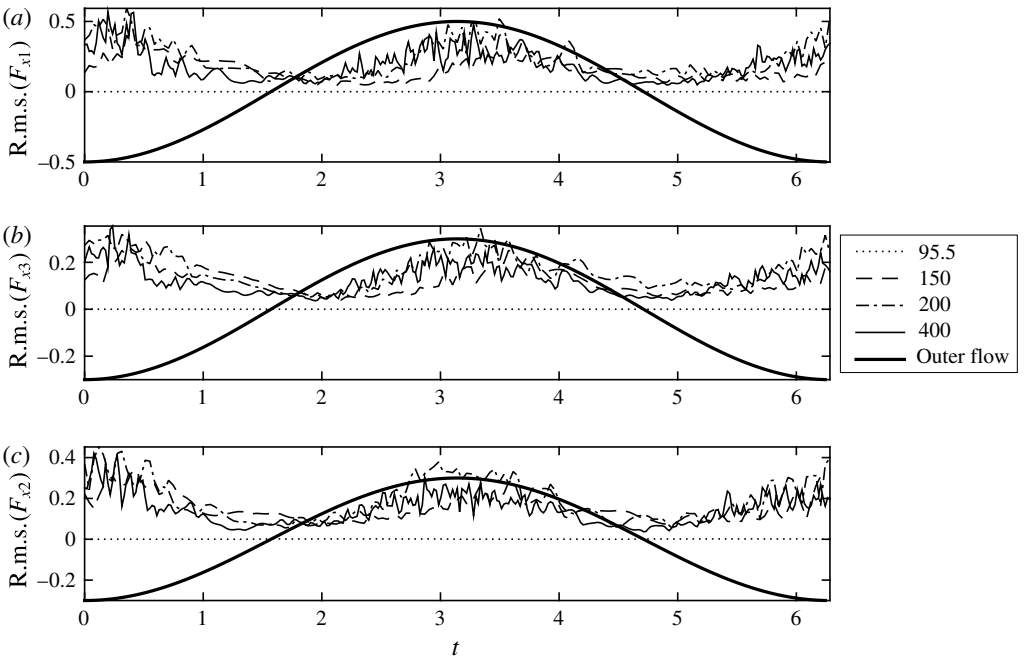


FIGURE 24. The r.m.s. values of the force components versus time for configuration A ($D = 6.95$): (*a*) r.m.s. of the streamwise force component; (*b*) r.m.s. of the cross-stream force component; (*c*) r.m.s. of the spanwise force component. The thick line indicates the time development of the velocity outside the boundary layer.

sphere are observed for configuration A, starting from $R_\delta = 150$, and for configuration B for $R_\delta = 600$ and for $R_\delta = 500$ in the third oscillatory cycle (see figures 24 and 25).

Looking at both figure 26 and figure 24, it can be concluded that, when the flow falls in the hydrodynamically rough turbulent regime, the variability in the force measured on the spheres is largest during the late accelerating and early decelerating phases. When the flow falls in the transitional turbulent regime, observed in configuration B for $R_\delta = 600$ and for $R_\delta = 500$ (third cycle), the differences in the forces on each sphere are mainly confined to the decelerating phases of the cycle (see figures 27 and 25). Moreover, in the transitional regime, the force on each sphere can be significantly larger than the mean value (see figure 27).

4. Conclusions

Direct numerical simulation of the oscillatory flow close to a wall covered with spherical roughness elements has allowed us to identify three flow regimes, which are named the laminar, transitional turbulent and hydrodynamically rough turbulent regimes. The transition from one regime to the other depends on the Reynolds number and on the diameter of the spheres covering the bed. In configuration A ($D = 6.95$) only the laminar and the hydrodynamically rough turbulent regimes are observed, while in configuration B ($D = 2.32$) the laminar and the transitional turbulent regimes are observed.

https://doi.org/10.1017/jfm.2016.61 Published online by Cambridge University Press

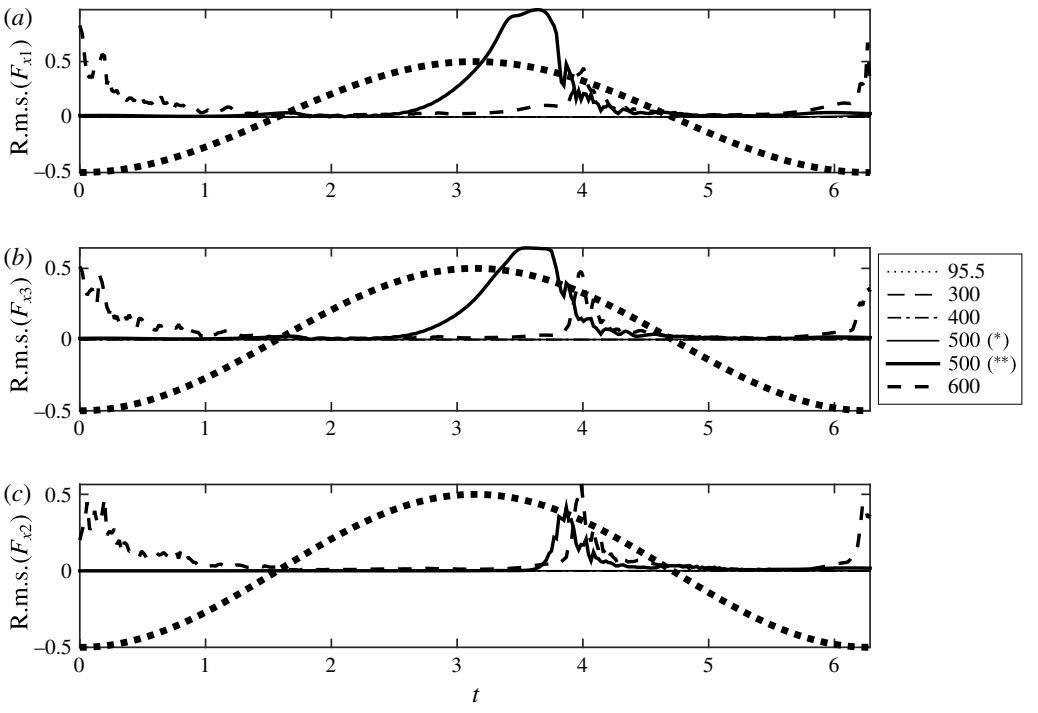


FIGURE 25. The r.m.s. values of the force components versus time for configuration B ($D = 2.32$): (*a*) r.m.s. of the streamwise force component; (*b*) r.m.s. of the cross-stream force component; (*c*) r.m.s. of the spanwise force component; (*) second oscillatory cycle; (**) third oscillatory cycle. The thick line indicates the time development of the velocity outside the boundary layer.

In the laminar regime, the turbulent kinetic energy attains negligible values, the force exerted on individual roughness elements has the same value and the vorticity dynamics appears to be related only to the interaction of the flow field with the roughness geometry.

As R_δ is increased and for configuration A ($D = 6.95$), the hydrodynamically rough turbulent regime is observed, disturbances start to grow and random fluctuations influence vorticity dynamics, particularly in the phases where the external velocity attains its largest values. The force exerted on the spheres shows different values from one sphere to another, particularly during the accelerating and early decelerating phases of the cycle.

The transitional turbulent regime is observed only for $D = 2.32$ and for the largest values of R_δ considered. The turbulent kinetic energy shows significant peaks during the decelerating phases of the oscillatory cycle and the vorticity dynamics is characterized by a large spatial variability, particularly during the decelerating phases. Vortex streaks form during the late accelerating phases. During the decelerating parts of the cycle, the streaks then break up, the vorticity is ejected far from the wall and the flow becomes turbulent. The force exerted on each sphere also shows a marked spatial variability during the decelerating phases. The critical value of the Reynolds number for transition from one regime to the other depends on D. Indeed, for configuration A transition occurs for R_δ between 95.5 and 150, while

https://doi.org/10.1017/jfm.2016.61 Published online by Cambridge University Press

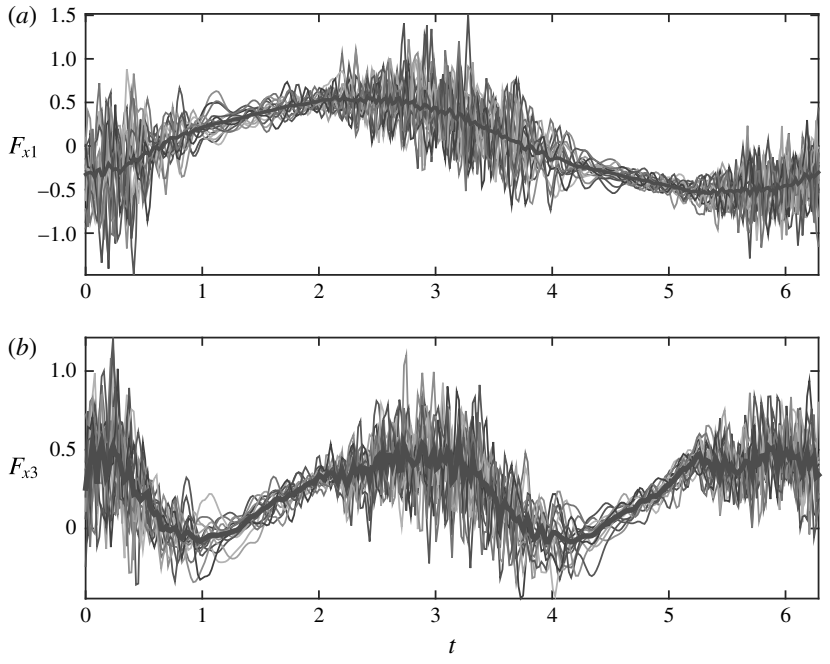


FIGURE 26. The force components F_{x1} and F_{x3} on each sphere of configuration A ($D = 6.95$) for $R_\delta = 400$. Thick line: average value.

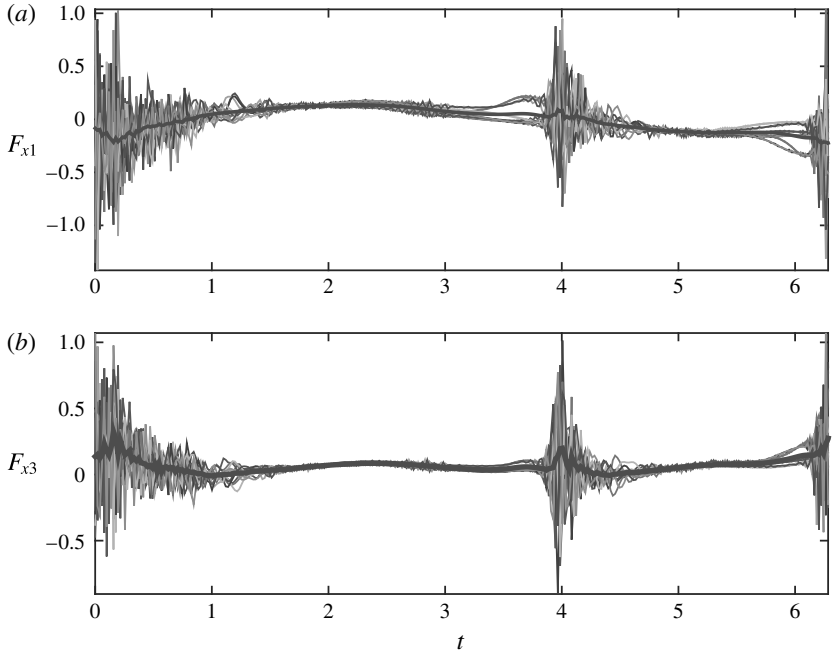


FIGURE 27. The force components F_{x1} and F_{x3} on each sphere of configuration B ($D = 2.32$) for $R_\delta = 600$. Thick line: average value.

https://doi.org/10.1017/jfm.2016.61 Published online by Cambridge University Press

for configuration B transition occurs for R_δ close to 500. The different critical values of the Reynolds number in the two configurations might be related to the role of the roughness elements in the transition process. Indeed, for $D = 2.32$ the transition process, which takes place for a larger value of the Reynolds number, shows similarities with the transition over a plane smooth wall. However, in order to reach definite conclusions on the role of roughness elements in the transition process, a wider investigation of the parameter space is necessary.

Acknowledgements

This study has been possible thanks to computational resources provided by CINECA (Bologna, Italy, under the project IsC09_TOBL), by PRACE (project 2013081647) and by the Steinbuch Centre for Computing (KIT, Karlsruhe, Germany), to 'Ministero dell'Istruzione, dell'Università e della Ricerca' (under the research project n.2012BYTPR5 'Hydro-morphodynamic modelling of coastal processes for engineering purpose') and to the support of the University of Genova under the projects PRA2012 and PRA2013. The authors wish also to thank M. Uhlmann and the 'turbulent group' at KIT for their helpful comments during the development of the direct numerical simulation code. M.M. thanks the Deutscher Akademischer Austausch Dienst for having provided a scholarship (A1178248). Part of the software used in this work was developed by the DOE NNSA ASC- and DOE Office of Science ASCR-supported Flash Center for Computational Science at the University of Chicago.

Supplementary movie

A supplementary movie is available at http://dx.doi.org/10.1017/jfm.2016.61.

REFERENCES

ACARLAR, M. S. & SMITH, C. R. 1987 A study of hairpin vortices in a laminar boundary layer. Part 1. Hairpin vortices generated by a hemisphere protuberance. *J. Fluid Mech.* **175**, 1–41.

BLONDEAUX, P. 1987 Turbulent boundary layer at the bottom of a gravity wave. *J. Hydraul Res.* **25**, 447–464.

BLONDEAUX, P. & VITTORI, G. 1994 Wall imperfections as a triggering mechanism for Stokes-layer transition. *J. Fluid Mech.* **264**, 107–135.

CARSTENSEN, S., SUMER, B. M. & FREDSOE, J. 2010 Coherent structures in wave boundary layers. Part 1. Oscillatory motion. *J. Fluid Mech.* **646**, 169–206.

CARSTENSEN, S., SUMER, B. M. & FREDSOE, J. 2012 A note on turbulent spots over a rough bed in wave boundary layers. *Phys. Fluids* **24** (11), 115104.

COSTAMAGNA, P., VITTORI, G. & BLONDEAUX, P. 2003 Coherent structures in oscillatory boundary layers. *J. Fluid Mech.* **474**, 1–33.

DIXEN, M., HATIPOGLU, F., SUMER, B. M. & FREDSOE, J. 2008 Wave boundary layer over a stone-covered bed. *Coast. Engng* **55**, 1–20.

FORNARELLI, F. & VITTORI, G. 2009 Oscillatory boundary layer close to a rough wall. *Eur. J. Mech. (B/Fluids)* **28**, 283–295.

GHODKE, C., SKITKA, J. & APTE, S. V. 2014 Characterizaton of oscillatory boundary layer over a closely packed bed of sediment particles. *J. Comput. Multiphase Flows* **6**, 447–456.

HUANG, J. & GREENGARD, L. 1999 A fast direct solver for elliptic partial differential equations on adaptively refined meshes. *SIAM J. Sci. Comput.* **21** (4), 1551–1566.

JENSEN, B. L., SUMER, B. M. & FREDSOE, J. 1989 Turbulent oscillatory boundary layers at high Reynolds numbers. *J. Fluid Mech.* **206**, 265–297.

https://doi.org/10.1017/jfm.2016.61 Published online by Cambridge University Press

JEONG, J. & HUSSAIN, F. 1995 On the identification of a vortex. *J. Fluid Mech.* **285**, 67–94.

JIMENÉZ, J. 2004 Turbulent flows over rough walls. *Annu. Rev. Fluid Mech.* **36**, 173–196.

KEILLER, D. C. & SLEATH, J. F. A. 1976 Velocity measurements close to a rough plate oscillating in its own plane. *J. Fluid Mech.* **73**, 673–691.

MAZZUOLI, M., VITTORI, G. & BLONDEAUX, P. 2011 Turbulent spots in oscillatory boundary layers. *J. Fluid Mech.* **685**, 365–376.

OZDEMIR, C. E., HSU, T. & BALACHANDAR, S. 2014 Direct numerical simulations of transition and turbulence in smooth-walled Stokes boundary layer. *Phys. Fluids* **26** (4), 045108.

RICKER, P. M. 2008 A direct multigrid Poisson solver for oct-tree adaptive meshes. *Astrophys. J. Suppl.* **176** (1), 293–300.

ROSENTHAL, G. N. & SLEATH, J. F. A. 1986 Measurements of lift in oscillatory flow. *J. Fluid Mech.* **164**, 449–467.

SAFFMAN, P. G. 1970 A model for inhomogeneous turbulent flows. *Proc. R. Soc. Lond.* A **317**, 417–433.

SAFFMAN, P. G. & WILCOX, P. C. 1974 Turbulence models predictions for turbulent boundary layers. *AIAA J.* **12**, 541–546.

SLEATH, J. F. A. 1987 Turbulent oscillatory flow over rough beds. *J. Fluid Mech.* **182**, 369–409.

THOMAS, C., BLENNERHASSETT, P. J., BASSOM, A. P. & DAVIES, C. 2015 The linear stability of a Stokes layer subjected to high-frequency perturbations. *J. Fluid Mech.* **764**, 193–218.

UHLMANN, M. 2005 An immersed boundary method with direct forcing for the simulation of particulate flows. *J. Comput. Phys.* **209**, 448–476.

VANELLA, M., RABENOLD, P. & BALARAS, E. 2010 A direct-forcing embedded-boundary method with adaptive mesh refinement for fluid–structure interaction problems. *J. Comput. Phys.* **229**, 6427–6449.

VITTORI, G. & VERZICCO, R. 1998 Direct simulation of transition in an oscillatory boundary layer. *J. Fluid Mech.* **371**, 207–232.

ZHOU, Z., WANG, Z. & FAN, J. 2010 Direct numerical simulation of the transitional boundary-layer flow induced by an isolated hemispherical roughness element. *Comput. Meth. Appl. Mech. Engng* **199**, 1573–1582.

https://doi.org/10.1017/jfm.2016.61 Published online by Cambridge University Press